J. Fluid Mech. (2007), *vol.* 589, *pp.* 315–351.
doi:10.1017/S0022112007007793 Printed in the United Kingdom

Particle–fluid interactions in grid-generated turbulence

C. POELMA†, J. WESTERWEEL AND G. OOMS

Laboratory of Aero and Hydrodynamics, Delft University of Technology, Leeghwaterstraat 21, 2628 CA Delft, The Netherlands
c.poelma@tudelft.nl

(Received 25 October 2006 and in revised form 25 May 2007)

The effect of small particles on decaying grid-generated turbulence is studied experimentally. Using a two-camera system, instantaneous fluid-phase and particle-phase measurements can be obtained simultaneously. The data obtained with this system are used to study the decay behaviour of the turbulent flow. The role of particle size, particle density and volume load is studied in a number of different cases. These cases are chosen so that the individual role of these parameters can systematically be evaluated. Addition of particles to the flow has significant effects on the decaying turbulence: first, the onset of the turbulent decay appears to shift upstream; second, the flow becomes anisotropic as it develops downstream. The latter is observed as an increase in integral length scale in the vertical direction. The rate at which the flow becomes anisotropic can be predicted using a new parameter: the product of the non-dimensional number density and the Stokes number (referred to as the 'Stokes load'). This parameter, combining the relevant fluid and particle characteristics, is a measure for the energy redistribution leading to anisotropy. In addition to redistributing energy, the particles also produce turbulence. However, this only becomes evident when the grid-generated turbulence has decayed sufficiently, relatively far downstream of the grid. The turbulence production by particles can also account for the observed decrease in slope of the power spectrum, which leads to a 'cross-over' effect. The production of turbulence by the particles can be predicted using a model for the momentum deficit of the particle wakes. The validity of this approach is confirmed using conditional sampling of the fluid velocity field around the particles.

1. Introduction

Turbulent dispersed two-phase flows are widespread in both nature and industry. Examples in nature include sediment transport by rivers, rain clouds and sand storms. In industry, examples include the pneumatic transport of solids, fluid catalytic cracking and cyclonic dust collectors. An extensive overview can be found in e.g. Sommerfeld, Tsuji & Crowe (1997). Despite their abundance, a generally applicable theory or model for predicting the behaviour of particle-laden flows is currently not available. A thorough analysis is hampered by the lack of consistent experimental data available in the literature. Even for apparently straightforward metrics, such as e.g. the change in the turbulent kinetic energy of a flow when particles are added, contradictory results are reported in the literature. For an overview of experimental data, see e.g. Gore & Crowe (1989) or Poelma & Ooms (2006). The latter also gives

an overview of a number of analytical models and numerical studies that describe an important idealized case of particle-laden flows: homogeneous, isotropic turbulence.

In this paper, the influence of small suspended particles on a decaying, nearly homogeneous and isotropic turbulent flow is studied using simultaneous whole-field measurements of both the fluid and particle phase. Apart from obtaining single-point statistics such as changes in the turbulence level, dissipation rates and length scales, the whole-field character of the measurements can provide supporting evidence to explain the observed changes. An example of the need for whole-field measurements is the phenomenon of 'preferential concentration'. This effect, as observed for instance in experimental work by Eaton & Fessler (1994) and in a numerical study by Ferrante & Elghobashi (2003), is difficult to study using classic 'single-point' techniques. Here, whole-field velocity information can give direct insight into the interaction processes, rather than only measure the resulting integral quantities.

The focus of this paper is the so-called 'two-way coupling' regime (Elghobashi 1994): in this regime, the volume load is sufficiently high so that there is some kind of interaction between the particles and the fluid, yet the load is low enough to neglect particle–particle interactions.

1.1. *Background*

The difficulty in predicting particle–turbulence interaction arises from the large number of physical quantities that are involved. In principle, the system is described by the amount of dispersed phase present, the dispersed-phase characteristics (size, density) and the turbulence characteristics (length, time and velocity scales). However, these primary parameters are in practice not sufficient. Many 'derived' quantities exist such as the response time of a particle (τ_p, usually derived using Stokes's drag law) and the terminal velocity (u_{TV}, also referred to as settling velocity). These parameters describing the particle behaviour are a function of the flow conditions, which indicates the entanglement of the governing physical properties; their exact relationship is still poorly understood.

From all these quantities, a number of dimensionless numbers can be derived, such as the ratio of the characteristic time of a particle and a turbulence time scale, commonly referred to as the Stokes number. Another example is the ratio of the terminal velocity of a particle and a typical fluid fluctuation ($\beta \equiv u_{TV}/u'$), which can be used to evaluate the influence of gravity (Yang & Shy 2005). Many different regimes exist in particle-laden turbulence, but a precise classification or prediction is currently difficult. In table 1 a non-exhaustive list is given of some parameters that are commonly used in the literature, together with a very brief description of their use. This list is given primarily to show the many different approaches found in the literature, while none of these parameters has emerged as being 'conclusive'.

The two most commonly used parameters mentioned in table 1, apart from the volume load, are the Stokes number and the ratio of particle size and fluid length scale, d_p/Λ (Gore & Crowe 1989). The Stokes number describes the ability of a particle to follow fluid motions. Very small values indicate 'tracer'-like behaviour of the particles, whereas for large values the particles will hardly be affected by the fluid motion. An interesting phenomenon occurs at values in the range of 0.1 to unity. Here, particles can only follow certain fluid motions, leading to 'preferential concentration' or 'clustering' effects (Eaton & Fessler 1994). Most theoretical models implicitly assume a homogeneous distribution of particles; it is currently not known exactly to what extent these non-homogeneities affect particle–fluid interaction.

Symbol	Parameter, description
Φ_v, Φ_m	particle volume, mass load (Elghobashi 1994) $\Phi_v < 10^{-6}$: one-way coupling (fluid→particles) $10^{-5} < \Phi_v < 10^{-2}$: two-way coupling (fluid↔particles) $\Phi_v > 10^{-2}$: four-way coupling (fluid↔particles, particles↔particles)
$\delta/d_p \approx 0.5\Phi_v^{-1/3} - 1$	mean spacing between randomly distributed particles $\delta/d_p \gg 1$: inter-particle collisions negligible $\delta/d_p < 10$: particle–particle interactions (hydrodynamic, collisions)
d_p/Λ	particle size vs. fluid integral length scale (Gore & Crowe 1989) $d_p/\Lambda > 0.1$: turbulence augmentation $d_p/\Lambda < 0.1$: turbulence attenuation
$Re_p = u' d_p/\nu$	particle Reynolds number, using fluid fluctuation
$Re_{TV} = u_{TV} d_p/\nu$	particle Reynolds number, using terminal velocity $Re_{TV} < 100$: turbulence attenuation (Hetsroni 1989) $Re_{TV} > 400$: turbulence generation
$St_p = \tau_p/\tau_K$	particle Stokes number $St_p \ll 1$: particle follows all fluid motions ('tracer') $St_p \gg 1$: particle hardly responds to fluid motions $St_p \approx 0.1 - 1$: preferential concentration (Eaton & Fessler 1994) $St_p > 100$: turbulence enhanced (Elghobashi 1994) $St_p < 100$: turbulence dampened

TABLE 1. Overview of some commonly used parameters to describe dispersed two-phase flows.

The second parameter, d_p/Λ, has been obtained using a significant amount of experimental data and predicts with reasonable accuracy whether particles will increase or decrease the turbulence level. Similar criteria for predicting turbulence augmentation versus attenuation have been introduced by e.g. Hetsroni (1989), who used the Stokes number, and Elghobashi (1994), who used the particle Reynolds number. In practice, it is far from straightforward to vary a single parameter such as the Stokes number, while keeping all other parameters in the experiment constant. For instance, a particle with a higher Stokes number (in the same flow conditions) will automatically be more susceptible to gravitational forces, so that the ratio u_{TV}/u' also changes. This obviously complicates a systematic study, since observations cannot be linked directly to changes of a single parameter.

1.2. *Earlier work*

The influence of particles on turbulent flows has been studied extensively. However, most experimental work has been done in (fully developed) pipe flows, see e.g. Tsuji & Morikawa (1982), Kiger & Pan (2002) and Kussin & Sommerfeld (2002). In this case there is a continuous generation of turbulent kinetic energy at the wall. Though the quasi-steady nature of such a system may simplify the measurements, the inhomogeneity and anisotropy complicate a physical interpretation in terms of e.g. only two-way coupling effects. Additionally, in the work using horizontally oriented pipes, there is often a strong gradient in the local particle density (Kiger & Pan 2002).

Work using grid-generated turbulence has been performed by Schreck & Kleis (1993), Geiss *et al.* (2004) and Hussainov *et al.* (2000). The first used a vertical water channel, while the latter two studied an air/solid system. All three found that, even for a relatively modest volume load, there is an overall decrease in turbulent kinetic energy. Moreover, the flow appeared to become more anisotropic downstream of the grid (Geiss *et al.* 2004).

Related experimental work worth mentioning are studies of the effective settling velocity of particles in a homogeneous isotropic turbulent flow by e.g. Aliseda *et al.* (2002) and Yang & Shy (2005). These studies are closely related, but their focus is on different aspects of two-way coupling (i.e. the change in the settling velocity of a particle due to turbulence). Similarly, studies have been performed to primarily investigate the so-called clustering of particles due to the interaction of fluid and particles (Eaton & Fessler 1994). Finally, we mention work relating to the production of turbulence by particles falling in a quiescent medium, see e.g. Parthasarathy & Faeth (1990) and Lee, Faeth & Chen (2003). The interaction of particles with a turbulent fluid often entails both damping of turbulence and production of turbulence due to particles (commonly at different scales). The 'falling particles' experiments can help to give insight into two-way coupling phenomena by effectively eliminating one aspect of the interaction (i.e. the turbulent ambient fluid), so that the turbulence production can be studied in detail.

Apart from these experimental studies, there have also been a number of numerical studies of particle–fluid interaction in turbulent flows. Owing to the very high numerical demands, most of these have used a number of simplifications: the dispersed phase is often modelled as point particles (Elghobashi & Truesdell 1993; Boivin, Simonin & Squires 2000). Rather than solving the full equation of motion of the particles, it is usually considerably simplified by considering cases with a large density ratio (Squires & Eaton 1990; Ferrante & Elghobashi 2003). More recently, fully resolved simulations with finite particle diameter have become possible. These studies give insight into the fundamentals of the interaction between a single particle and its turbulent surroundings. Examples of this can be found in e.g. Bagchi & Balachandar (2004) and Burton & Eaton (2005). However, to date results of a fully resolved direct numerical simulation with moderate particle load such as reported in this study have not been published.

1.3. *Scope and outline of this paper*

It is not feasible to study all relevant aspects of the two-way coupling between particles and a turbulent fluid in a single study. In this study, the focus will be on the effects that the particles have on the continuous phase. In particular, we will study the decay rate of the turbulence. In § 2, the experimental facility will be described, together with a characterization of the single-phase flow in this facility. Subsequently, particles will be added to this flow to study their effect on the decay rate (§ 3). In § 4, a number of cases will be studied to clarify the role of some parameters, such as particle size, particle density and mass/volume load. As indicated in the introduction, the exact role of these parameters is not yet understood. By a careful selection of combinations, such as two experiments with identical mass load, yet with different volume load, their exact role can be clarified. The motivation for the choice of the experimental conditions is described in § 3.1. The outcome of these experiments will also be used to evaluate a number of the rules-of-thumb mentioned in § 1.2.

We will use the turbulence power spectrum to investigate the physical basis of the observed results, i.e. to clarify the coupling effects between the two phases. This approach also allows a direct comparison with earlier studies, some of which have hinted at a so-called 'cross-over' in the spectrum. This 'cross-over' or 'pivoting' effect refers to an observed decrease in energy at large scales, combined with an increase at energy at small scales. One physical explanation given for this effect assumes that particles take up energy from large-scale fluid motions (thus damping energy in this part of the spectrum), while they release it at smaller scales, due to e.g. wake shedding

(adding energy at higher wavenumbers). While many models exist that aim to predict the overall change in turbulent kinetic energy (Yuan & Michaelides 1992; Yarin & Hetsroni 1994; Geiss *et al.* 2004), only a few theoretical models try to describe the underlying changes in the turbulence structure in detail. For instance, L'vov, Ooms & Pomyalov (2003) derived a single-fluid model for homogeneous isotropic turbulent suspensions. They accounted for the coupling between particles and fluid by introducing a wavenumber-dependent effective density and a wavenumber-dependent damping term that expresses the (Stokes) drag between fluid and particles. They found that the particles decrease the effective kinematic viscosity of the suspension, so that the inertial subrange of the spectrum is elongated. In combination with the damping at large scales, this can lead to the observed pivoting.

The pivoting effect has so far been observed in a number of numerical studies (Boivin, Simonin & Squires 1998; Sundaram & Collins 1999*b*; Ferrante & Elghobashi 2003; Ten Cate *et al.* 2004). Theoretical models have been proposed that can predict it (L'vov *et al.* 2003; Ooms & Poelma 2004; Ooms & Poesio 2005). However, experimental verification of this phenomenon, mainly using experiments involving grid-generated turbulence, has so far been ambiguous. For a more thorough discussion of previous experimental work see the review by Poelma & Ooms (2006) here we will only report the main conclusions: Schreck & Kleis (1993) found a small decrease at large scales and an increase at small scales for neutrally buoyant particles in water for the longitudinal spectrum. Hussainov *et al.* (2000) also found a very small increase at small scales, yet no change at large scales. Geiss *et al.* (2004) performed comparable experiments, but did not find any changes in the spectrum. A study by Yang & Shy (2005) describes particle–turbulence interaction in stationary homogeneous and isotropic turbulence. They find significant changes in the shape of the spectra, depending on the Stokes number of the particle: (1) for small particles ($St_p = 0.36$), they find an attenuation at large scales and augmentation at scales larger than the Taylor microscale (in both the horizontal and vertical velocity spectrum), (2) for intermediate particles no changes are observed at large scales, while there is again an increase at scales larger than the Taylor microscale (again both horizontal and vertical), (3) for heavy particles ($St_p > 1.9$), the large scales are damped and small scales are augmented in the horizontal direction, while all scales are augmented in the vertical direction.

It should be noted that direct comparison between these experiments is difficult, owing to the differences in particle types and mass and volume loads, measurements techniques and data presentation (especially the choices for the normalization of the spectrum).

1.4. *Flow geometry and conditions*

The flow geometry that is chosen for this study is grid-generated turbulence. This type of flow is nearly homogeneous and isotropic and therefore it allows great simplifications in mathematical as well as physical analyses (Pope 2000). Many well-documented classic single-phase experiments are available in the literature that can serve as reference cases for the current measurements (Batchelor & Townsend 1948; Van Atta & Chen 1968; Comte-Bellot & Corrsin 1971; Sirivat & Warhaft 1983).

The mean flow direction is chosen to be vertical, so that no gravity-induced concentration inhomogeneities are to be expected. Again, this simplifies the problem under investigation, because of the increased symmetry.

For the choice of combinations of continuous and dispersed phase, several possibilities exist. For the dispersed phase, we decided to use small solid particles,

rather than small (liquid) droplets, because, any uncertainty in the size distribution due to e.g. coalescence or breakup can be eliminated. The particles are furthermore chosen to be roughly spherical. For the continuous phase, a gaseous or liquid phase can be chosen. Here, water is chosen as working medium, for several reasons. In solid/liquid systems, the slip velocity (i.e. the difference in mean convective velocity of the two phases) is lower than in solid/gas systems. Furthermore, the time scales of the fluid phase are larger than in air. Both these effects have significant advantages in the design of the measurement system. As will be discussed in a subsequent section, the measurement technique requires the use of relatively large fluorescent tracer particles. The use of water and the corresponding relatively large time scales are better suited for the relatively large response times of these particles. Furthermore, they are more easily distributed in a liquid flow due to less settling.

Apart from these practical considerations, there are a number of physical consequences of these choices. The most important consequence results from the density ratio of the order of unity. For small particles in air, significant simplifications can be made for the particle equation of motion. The most complete description is the Basset–Boussinesq–Oseen (BBO) equation (Maxey & Riley 1983). This equation contains some rather challenging terms, especially the 'history' term, describing the unsteady drag, but for small particles in air it reduces to three terms: the change in particle momentum, buoyancy and Stokes drag. However, for particle–fluid systems with a density ratio of order unity, it is *a priori* not known which terms of the BBO equations can be neglected. This highlights the need for detailed measurements, especially in this regime.

2. Experimental methods

2.1. *Flow facility*

Turbulence is generated by placing a grid in a vertical recirculating water channel, see figure 1. The mean flow is in the upward direction. The grid consists of a perforated plate with $7.5 \times 7.5\,\mathrm{mm}^2$ square holes with a total solidity of 0.45. It is placed upstream of a glass circular test section with a diameter of 0.10 m and length of 0.66 m, which is enclosed in a rectangular glass box to limit optical distortion by curved media transitions. Grid-generated turbulence is slightly anisotropic, which is compensated by using a sudden 1:1.11 area ratio contraction (Comte-Bellot & Corrsin 1966). Typically, the mean flow velocity ($U \equiv \overline{u_z}$) is $0.5\,\mathrm{m\ s}^{-1}$, corresponding to a bulk Reynolds number of 50×10^3 and a mesh-size-based Reynolds number of 3750 (details of the flow will be discussed in § 2.5 and summarized in table 2). The mean mass flow rate is measured using an electromagnetic flow meter (Krohne Altoflux), which is placed in the return pipe.

Particles are introduced at the top and recycled through the facility during the measurements. They can be removed by placing a fine filter in the return pipe. This filter captures the dispersed phase (typically larger than 200 μm), while the tracer particles (approximately 20 μm) can pass through the filter. This filter is enclosed by two ball valves, so that the water and tracer particles can remain in the facility when the dispersed phase is replaced.

2.2. *Volume load measurements*

Owing to the relatively large size and complexity of the experimental facility, it is difficult to estimate the actual particle volume load in the test section based purely on the system volume and the number of particles that has been introduced. Because

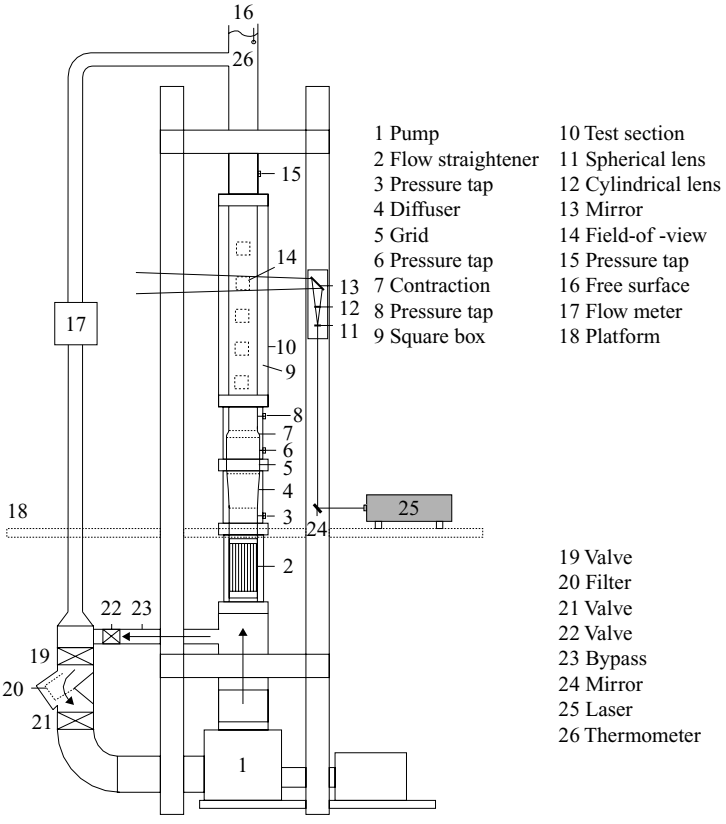

FIGURE 1. Schematic drawing of the vertical water channel with turbulence-producing grid.

of e.g. sedimentation in corners, the particles will most likely not be distributed homogeneously over the entire system. Therefore, a method to determine the actual volume load during the measurements is desirable. This is done by measuring the increased pressure drop over the test section compared to the equivalent single-phase case. This observed pressure drop is due to wall friction effects and the hydrostatic pressure difference. The former is assumed to be unaffected by the presence of the particles. Though this assumption cannot be validated *a priori*, it is found that the required power input of the system, i.e. the pump setting to maintain a certain mean flow rate, hardly increased when particles were added. The latter is a result of the relatively low mass loads that are used. Additionally, the increase of the effective viscosity of the suspension (Landau & Lifshitz 1987) is negligible at the volume loads under consideration.

The hydrostatic pressure over the test section is determined by the effective density of the suspension:

$$\Delta p = \rho_{\mathrm{eff}} g h, \quad \text{with} \quad \rho_{\mathrm{eff}} = \Phi_v \rho_p + (1 - \Phi_v)\rho_f. \tag{2.1}$$

Using the height difference between two pressure taps (h), the observed pressure difference (Δp) and the single-phase reference pressure drop (Δp_{sp}), the volume load can be determined using

$$\Phi_v = \frac{\Delta p - \Delta p_{\mathrm{sp}}}{(\rho_p - \rho_f) h g}. \tag{2.2}$$

The accuracy of this method is limited by the error in the pressure difference method. In this study, the pressure drop over the test section is measured using a differential membrane transducer. One side of this transducer measures the total pressure drop over the test section, while the other side measures a column of water of exactly the same height. Owing to this differential nature of the measurement, the relatively small changes in the pressure drop (of the order of 50–100 Pa) due to the particles can still be measured with reasonable accuracy (estimated at 5 Pa based on repeated calibrations and single-phase experiments). A moving average over 15 s is used to smooth out high-frequency fluctuations.

The accuracy of the load measurement is proportional to the density difference: the accuracy in pressure measurement corresponds to an error in the volume load of 0.019% for ceramic particles, while the error for glass particles is of the order of 0.035% (see the next section for particle details). These errors are relatively large, but still an order of magnitude smaller than the volume loads used in this study. For relatively light particles (for which no settling is expected), the volume load obtained from the pressure drop agreed well (within 10–15%) with estimates based on the total mass of particles added to the total system volume.

Alternatively, the volume load could have been determined using optical measurements (e.g. light transmission/attenuation). The problem with this method is that the calibration is very elaborate, since very controlled, homogeneous volume loads have to be maintained *in situ*, for each particle type and size separately. The pressure method does not need a calibration, apart from the single-phase pressure drop at the desired flow rate.

2.3. *Measurement techniques*

Simultaneous fluid- and particle-phase measurements are obtained using a dual-camera particle image velocimetry (PIV) system specifically developed for this facility. A detailed description can be found in e.g. Poelma (2004) and Poelma, Westerweel & Ooms (2006). Here, only a general description will be given.

The measurement system consists of two cameras that are focused on the same field of view, using a mirror and a beam splitter plate, see figure 2. To ensure that each camera only records one phase, tracer particles containing fluorescent dye and an appropriate wavelength cutoff (i.e. 'colour') filter are used. Previous applications of a similar approach can be found in e.g. Lindken & Merzkirch (2002) and Deen, Hjertager & Solberg (2000), both in bubbly flows.

The measurement volume is illuminated using a pulsed Nd:YAG laser (New Wave, 20 mJ/pulse @ 532 nm, light sheet thickness approx. 0.5 mm). The scattered light from both particle types (tracer and dispersed phase) are captured on one of the two cameras (Roper Scientific ES4.0, 2048×2048 pixels, both fitted with 105 mm $f/2.8$ Micro Nikkor lenses). The tracer particles are more than an order of magnitude smaller than the dispersed phase, so their images cannot be distinguished from the background noise of the 'particle' camera, while the dispersed-phase particles will be clearly visible. In fact, the strong scattering of the dispersed particles requires the use of a neutral density (nd) or 'grey' filter to avoid over-exposure even at very small apertures. The tracer particles contain fluorescent dye (Rhodamine 6G), so that they will emit light at a higher wavelength than the original laser wavelength. By placing a wavelength cutoff filter in front of the second ('fluid') camera, reflections and scattering at the original wavelength can be blocked, while the fluorescent light from the tracer particles will pass through. Visual inspection of the images from each camera indicated that indeed no 'cross-talk' between the two phases occurred.

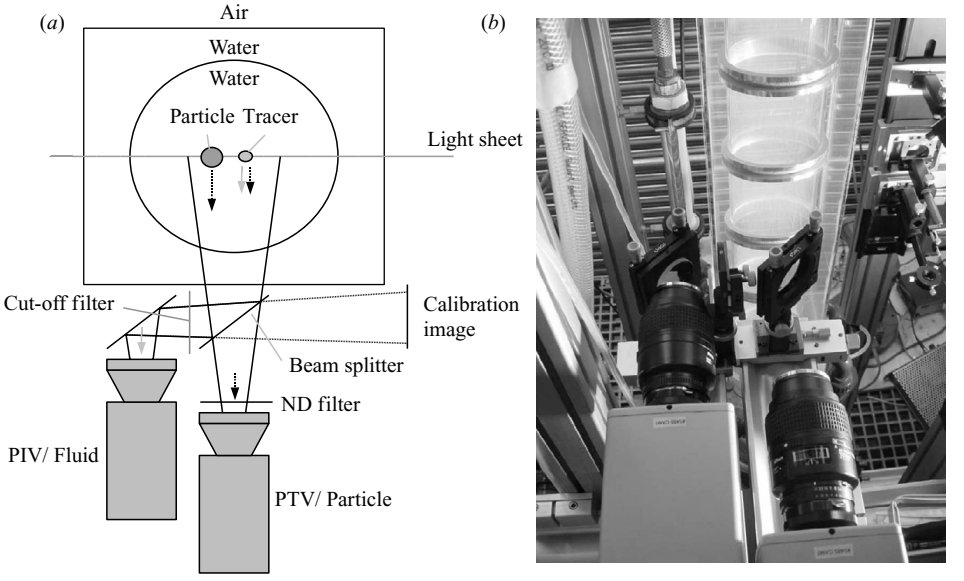

FIGURE 2. (*a*) Schematic illustration and (*b*) photograph of the simultaneous measurement of the fluid and dispersed phases using fluorescent tracer particles.

Using this optical system, each camera records a pair of images with a short time delay, determined by the laser pulse delay time ΔT, which is typically 1500–2000 μm, depending on the flow conditions. Increasing the delay time leads to a larger dynamic range of velocity. However, a too long delay time results in loss of correlation due to out-of-plane motion. The choice for the optimum delay time is discussed in detail in Poelma *et al.* (2006). These image pairs are subsequently processed to obtain the particle- and fluid-phase velocities, respectively. Because the two image pairs have very different characteristics (e.g. particle size, number density), each of the pairs is processed with a dedicated processing technique.

The number of dispersed-phase particles in each image is relatively low (of the order of 100). Therefore, a particle tracking velocimetry (PTV) algorithm is most suitable for these images (Raffel, Willert & Kompenhans 1998). For these images, the 'particle mask correlation' algorithm was found to be the most suitable (Kiger & Pan 2000; Poelma 2004). In this algorithm, particles are detected by cross-correlating the images with a 'mask' or model particle. This mask is a two-dimensional Gaussian grey-value distribution; the size of this mask is estimated from the real images (typically 10–20 pixel). The cross-correlation will yield the locations of the particles in both frames, evident as local maxima in the correlation result. From Gaussian peak fits to each of these local maxima, the particle locations can be obtained with subpixel accuracy. The corresponding particles in both frames are matched using a simple nearest-neighbour approach. This method is well suited for these images, since the fluctuating component of the displacement of the particles is significantly smaller than the mean particle spacing.

The fluid-phase images have a significantly higher number density than the particle-phase images. Therefore, they are more suited for processing using particle image velocimetry (PIV) (Willert & Gharib 1991). In PIV, the local fluid velocity is estimated from the displacement of groups of tracer particles in small segments of the total image, the so-called interrogation areas. The displacement is generally estimated by

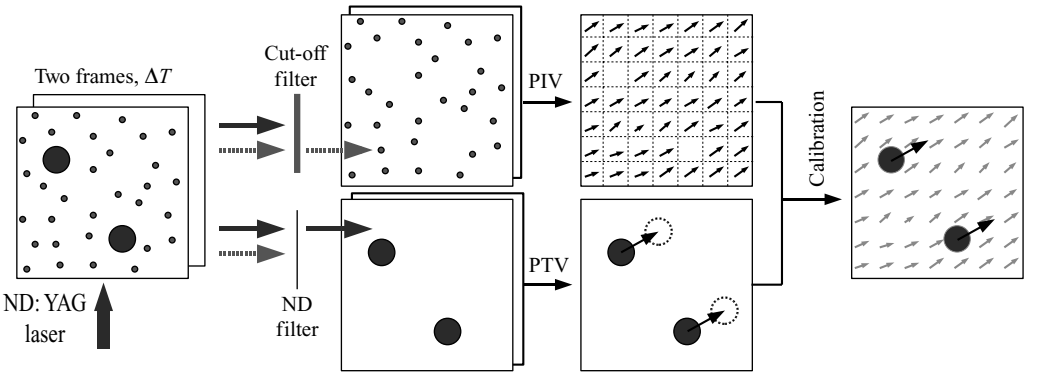

FIGURE 3. Schematic representation of the data processing to obtain simultaneous velocity measurements of the fluid and particle phases.

cross-correlating the interrogation areas and subsequently determining the location of the maximum in the correlation field ('displacement peak'). In this study, a three step analysis is performed: an initial estimate using interrogation areas of 64×64 pixels and subsequently two iterations using 32×32 pixels. No overlap of the interrogation areas is used to avoid oversampling effects due the relatively low number density, which was a result of the presence of the dispersed phase, which is described in detail by Poelma *et al.* (2006).

After obtaining the velocity measurements of both phases, they have to be combined. We have implicitly assumed until now that the cameras are focused on the same field of view. In practice, it is very difficult to get an exact overlap of the two recorded images owing to the relatively high magnification factor and the large total number of degrees of freedom of the optical components. To overcome this problem, we use the 'disparity' approach (Willert 1997). The overlap of the two cameras is optimized as much as possible using a calibration image. Using local cross-correlation similar to a PIV analysis these two images are then compared. This will yield the local disparity field of the two images, which is used to 'map' one of the images onto the other. This correction was always smaller than 10–15 pixels (equivalent to 0.18–0.27 mm), i.e. lower than the spatial resolution of the fluid-phase result (discussed below).

The measurement process is represented schematically in figure 3. The hardware control and data acquisition is done using a commercial LaVision Flowmaster system (running DaVIS 6.0). The images are processed using in-house software (Westerweel 1993; Poelma 2004).

In figure 4 a typical example of a single 'snapshot' of the flow using the system is given: the disks represent particle locations, while the bold vectors indicate their velocity. The vectors on the regular grid (64×64) represent the local fluid velocity. Note that the mean velocity of both phases has been subtracted in this figure for clarity (note that the mean slip velocity is in fact significantly larger than the fluid fluctuations). The vector spacing is 0.63 mm, roughly twice the Kolmogorov length scale λ_k as determined using laser Doppler anemometry in earlier experiments. This in-plane resolution is comparable to the light sheet thickness of 0.5 mm. The total field of view is approximately 4×4 cm^2, approximately eight times the integral length scale, Λ. Measurements can only be recorded with a frequency of 0.5 Hz, while the eddy turnover time ($T = \Lambda/u'$) is estimated at 0.5–1.0 s. Therefore, the temporal

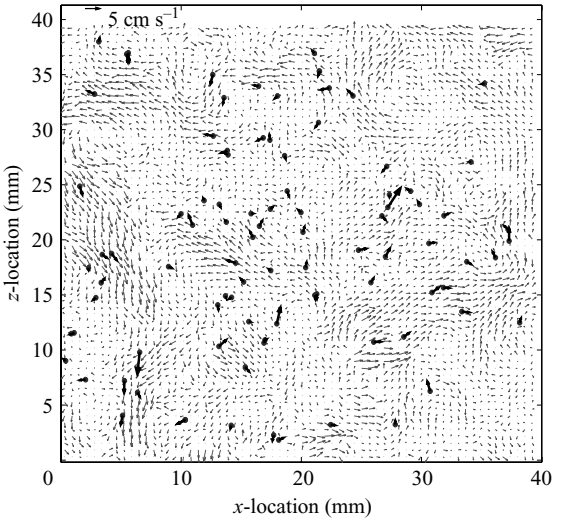

FIGURE 4. Example of a simultaneous recording of both fluid and particle velocities. Vectors on the regular grid represent fluid velocities, disks and bold vectors represent the particle locations and velocities.

development of the flow cannot be studied. The results reported in this study are based on the statistics of 128 or 512 statistically independent measurements. Measurements are performed at five downstream locations ($z/M = 43-100$, with z the distance from the grid and M the grid size) for each flow condition (e.g. particle size, load).

2.4. *Data processing*

In dispersed two-phase flows, it is inevitable that some signal loss occurs. In preliminary experiments, it was found that generally 10–20% of the PIV data were missing even at a moderate particle volume load of 0.5%. The missing data are a result of the reduced image quality due to the presence of the dispersed phase: particles in front of the light sheet block the light emitted by the tracer particles. Therefore, the observed tracer density decreases dramatically (Poelma *et al.* 2006). This leads to a higher noise level in the correlation plane and thus to more spurious vectors in the PIV result. The decrease in tracer density is also the reason why no overlapping interrogation areas are used in this study (as mentioned earlier), since there is an increased chance of oversampling and associated bias.

To obtain turbulence statistics from the PIV/PTV measurements, the autocorrelation functions of the velocity data are calculated. This is done using the 'slotting' method originally developed for the processing of non-equidistant data obtained using laser Doppler anemometry (Tummers & Passchier 2001). It has been shown that it can readily be applied to PIV data too (Poelma *et al.* 2006). Also, the method has been extended so that it can process unstructured data (i.e. not on a regular grid, such as obtained from e.g. PTV). The idea behind the method is that the autocorrelation function of a signal is constructed by an explicit multiplication of all possible combinations of the data records. Subsequently, these products are sorted according to their spatial or temporal separation and averaged for discrete 'slots' to obtain a smooth estimate for the covariance function, which can be normalized using the variance to obtain the autocorrelation function.

The advantage of the slotting method is that it gives improved estimates for the turbulence statistics, because there is no need for interpolation of any missing data, required if conventional methods are used (e.g. using Fourier transforms to obtain a power spectrum). Interpolation gives rise to bias, especially if the percentage of signal drop-out is more than 10%. This bias affects the shape of the spectrum up to length scales an order of magnitude larger than the vector spacing. More importantly, the bias effects on these small scales can even contaminate integral quantities if noise correction techniques are used. For example, a commonly used technique is fitting a parabola to the autocorrelation function to remove uncorrelated noise, giving a better estimate for the variance of a signal, see e.g. Benedict & Gould (1998). With significant signal loss, this variance will be biased (generally it will be overestimated), but also 'derived' quantities such as the Taylor microscale, the dissipation rate, etc. are affected (Poelma *et al.* 2006).

Two implementations of the slotting method are used in this work: the 'row-by-row' approach for PIV data and the 'decomposition' approach for PTV data. Here, they will only be discussed briefly; a more detailed description can be found in Poelma *et al.* (2006). Both implementations use the same principle, but they are optimized for the data under consideration (respectively data on a regular grid and sparse unstructured data). In the 'row-by-row' approach, one covariance function is reconstructed by adding the contributions from each row of vectors, for all realizations. This results in a spatially and temporally averaged covariance function of the quasi-steady flow, using typically up to 2 million vectors for each measurement location and condition. The assumption of quasi-stationarity and homogeneity was supported by earlier measurements using laser Doppler anemometry (Poelma 2004). In the 'decomposition' approach, all possible combinations of particle velocity vector pairs in one realization are decomposed into transversal and longitudinal components. Subsequently, these are processed using the slotting method, i.e. their multiplications are added to find an average covariance function. Typically, up to 50 000 dispersed-phase particle velocities are available.

From the covariance function, all turbulence statistics that will be reported in the next sections can be derived (Pope 2000). More importantly, the particle statistics can be analysed in a similar manner. For instance, the particle correlation function can be used to determine length scales and to correct the variance in the fluctuations of the particles (by removing uncorrelated noise, as mentioned above). The latter is critical since the error in the velocity obtained for a single (dispersed-phase) particle is typically an order of magnitude higher than for an ensemble of tracer particles (Poelma 2004). Therefore, the energy contained by the particle phase is overestimated significantly if this correction is not applied.

2.5. *Single-phase flow*

As a reference for the particle-laden measurements, the flow in the facility is first characterized for the single-phase case. This is done using the same measurement system as will be used for the two-phase flow, to ensure that any observed changes in turbulence statistics cannot be caused by the measurement method. As stated in § 1.4, single-phase grid-generated turbulence is relatively well-understood and there is a large body of experimental data available in the literature for comparison. We only report the main turbulence characteristics here, a more extensive discussion can be found in Poelma (2004).

The mean velocity profile in the centre of the test section was found to be flat: there was less than 1% deviation of the mean velocity (Poelma 2004). The boundary

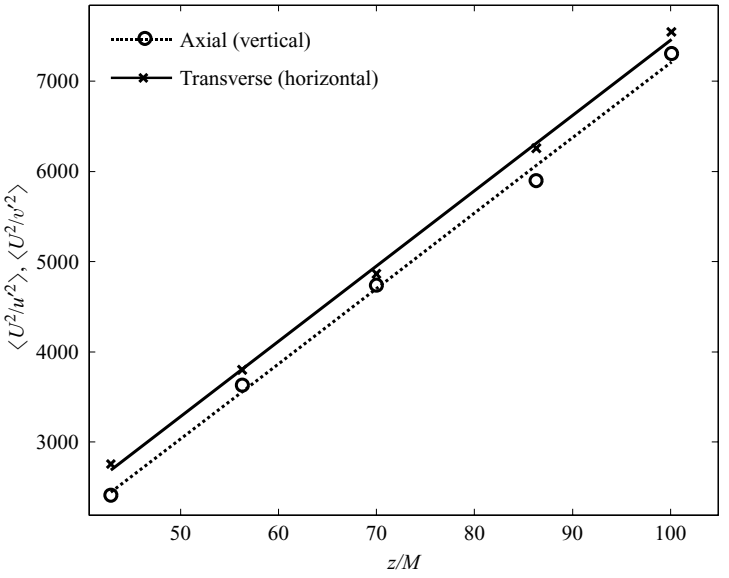

FIGURE 5. Decay of the turbulent kinetic energy for the single-phase case. Symbols represent PIV measurement data, the lines are power-law fits.

layer thickness (defined here as the distance from the wall to reach 95% of the mean axial centreline velocity) was 11 mm at the bottom of the test section, so that the centre of the pipe is sufficiently homogeneous; as mentioned earlier, the field of view is approximately $4 \times 4\,\mathrm{cm}^2$. The downstream growth of the boundary layer influenced the mean centreline velocity: at the exit of the test section it was 7% higher than near the entrance.

Figure 5 shows the development of the axial (i.e. vertical) and transverse (i.e. horizontal) variance of the fluid fluctuations (respectively $\langle u'_x u'_x \rangle$ and $\langle u'_z u'_z \rangle$, with $\langle \ldots \rangle$ denoting an ensemble average and a prime indicating the root-mean-square value), as a function of the dimensionless downstream distance (z/M). The variance of the velocity fluctuations is normalized using the mean centreline velocity, which is kept constant throughout all measurements at $U = 0.53\ \mathrm{m\,s^{-1}}$. As can be seen in the graph, the turbulence decays according to a power law (note that the reciprocal value of the variance is plotted) and the flow is nearly isotropic: the anisotropy ratio u'_z/u'_x decreases from 1.06 to 1.02 in the test section.

An overview of the relevant turbulence statistics at the five downstream locations is given in table 2. All of these parameters were derived from the autocorrelation function, as obtained from the PIV data using the slotting method. The integral length scale was calculated by integrating the longitudinal autocorrelation function. The second derivative of the transversal autocorrelation function at $r = 0$ was used to determine the Taylor microscale. The dissipation rate was calculated from the decay of the variance, as well as from the Taylor micro scale, using

$$\epsilon = 15\nu \frac{u'^2}{\lambda_g^2}. \tag{2.3}$$

Note that this equation is only valid for isotropic turbulence, i.e. $u'_{x,y} = u'_z$ (Pope 2000). Nonetheless, the results for the dissipation rate from these two methods were in

Downstream distance	z/M	42.9	56.3	70.0	86.3	100
Turbulence intensity	$I \equiv u'/U$ [%]	2.0±0.04	1.6	1.4	1.3	1.2
Integral/macro length scale	Λ [$\times 10^{-3}$ m]	4.9±0.37	5.7	6.0	6.7	7.4
Streamwise r.m.s. of fluctuations	u'_z [$\times 10^{-3}$ m s^{-1}]	10.8±0.22	8.8	7.7	6.9	6.2
Transverse r.m.s. of fluctuations	u'_x [$\times 10^{-3}$ m s^{-1}]	10.1±0.14	8.6	7.6	6.7	6.1
Anisotropy	u'_z/u'_x	1.06±0.019	1.02	1.01	1.04	1.02
Eddy turnover time, Λ/u'	T[s]	0.45±0.038	0.65	0.78	0.97	1.16
Dissipation rate, from decay	ϵ [$\times 10^{-5}$ m^2 s^{-3}]	18.9±1.76	11.4	7.14	4.42	3.19
Dissipation rate, from λ_g	ϵ [$\times 10^{-5}$ m^2 s^{-3}]	22.3	12.1	7.22	4.71	3.16
Kolmogorov length scale	λ_k [$\times 10^{-3}$ m]	0.27±0.007	0.31	0.34	0.39	0.42
Kolmogorov velocity scale	u_k [$\times 10^{-3}$ m s^{-1}]	3.7±0.09	3.3	2.9	2.6	2.4
Kolmogorov time scale	τ_k [$\times 10^{-3}$ s]	73±3.9	94	118	150	177
Taylor micro scale	λ_g [$\times 10^{-3}$ m]	2.8±0.025	3.1	3.5	3.9	4.3
Reynolds number	Re_λ	28.8±0.74	27.0	26.3	25.7	27.1

TABLE 2. Summary of single-phase PIV results at the five measurement locations; for the first location the 95% confidence interval is given.

good agreement, see table 2. From the dissipation rates, the Kolmogorov scales could be estimated using their definitions: $\lambda_K = (\nu^3/\epsilon)^{1/4}$, $u_K = (\epsilon\nu)^{1/4}$ and $\tau_K = (\nu/\epsilon)^{1/2}$.

The results reported in table 2 were also determined using laser Doppler anemometry (LDA). The differences between the results obtained using the two methods were typically of the order of 5%, which is similar to the confidence interval of the measurements (Poelma *et al.* 2006). More importantly, the results are in agreement with earlier grid-generated turbulence experiments and theory (Batchelor 1953; Comte-Bellot & Corrsin 1971). Examples of the consistency of the data are the power-law decay of the variances, the fact that the Reynolds number stays constant and the growth of the length scales proportional to $(z/M)^{1/2}$.

3. Two-phase measurements

3.1. *Particles and measurement conditions*

Five particle types were selected with a relative density ranging from nearly unity (polystyrene) to 3.8 (ceramic)† in the size range of 150–500 μm. The bottom limit of this size corresponds roughly to the Kolmogorov length scale. The upper limit was determined by practical considerations: denser and larger particles could not be suspended consistently in the current facility. The particles response time ranges from 4.4 ms to 35.3 ms, equivalent to Stokes numbers from 0.06 to 0.48 (based on the turbulence quantities of the single-phase flow at $z/M = 42$). In table 3, a summary is given of some of properties for the five different particle types used. Note that the values for U_{TV}, Re_{TV} and β are all based on experimental results. The measured terminal velocities were all significantly lower (up to a factor 2 for P1) than the values predicted using Stokes's drag law. This was to be expected, given the particle Reynolds numbers (see table 3). Using a standard drag coefficient curve these finite-Reynolds-number effects can be taken into account. These predictions were in good agreement with the observed terminal velocities.

† The polystyrene particles are 'expandable polystyrene' particles, supplied by Nova Chemicals, Breda, The Netherlands. Glass and ceramic particles were supplied by Würth Abrasives, Bad Friedrichshall, Germany.

Code	Material	Size [μm]	Density [kg m^{-3}]	τ_p [ms]	St_p	U_{TV} [cm s^{-1}]	Re_{TV}	$\beta \equiv u_{TV}/u'$
P0	polystyrene	275 ± 43	1050	4.4	0.06	0.47	1.3	0.44
P1	glass	509 ± 122	2450	35.3	0.48	5.87	29.9	5.54
P2	glass	254 ± 37	2450	8.8	0.12	3.66	9.7	3.45
P3	ceramic	280 ± 83	3800	16.6	0.23	6.04	16.9	5.70
P4	ceramic	153 ± 42	3800	5.0	0.07	2.46	3.76	2.32

TABLE 3. Summary of the properties of the used particle types. The particle sizes are reported as a symmetric range covering 90% of the particle sizes, centred around the (number)-mean particle diameter.

Exp.	ρ_p/ρ_f	d_p [μm]	Φ_v [%]	Φ_m [%]	Locations	n_p [cm^{-3}]
1	3.8	153	0.12	0.44	r1, r2,r3, r4	640
2	3.8	280	0.10	0.38	r0, r1, r2, r3, r4	87
3	2.5	254	0.26	0.65	r0, r1, r2, r3, r4	303
4	2.5	254	0.072	0.18	r0, r1, r2, r3, r4	83
5	3.8	280	0.18	0.67	r0, r1, r2, r3, r4	157
6	2.5	254	0.42	1.05	r0, r1, r2, r3	489
7	2.5	509	0.37	0.92	r0, r1, r2, r3, r4	54
8	1.035	275	0.08	0.08	r0, r1, r2	285

TABLE 4. Summary of main experiments performed (see text for details). The mass/volume load of the neutrally buoyant particles could not be measured. Therefore, the amount added was divided by the total system volume to obtain an estimate. This was typically within 25% of estimations using the observed number density in the images.

In total, eight experiments were performed using various particle types and loads. In table 4, the conditions are reported for each experiment. The goal was to set up a range of experiments in which a number of direct comparison could be made. For instance, experiments 1 and 2 have the same mass and volume load, yet different particle sizes. Experiments 5 and 3 have the same mass load, same particle size, yet a different particle density (and thus different volume load). As a final example, experiments 2 and 4 have a comparable particle size and volume load, yet a different mass load. As can be seen in the table, the mass and volume loads are not exactly identical. In practice, it was difficult to accurately predict the effective mean load beforehand: particles had to be added and removed iteratively, which was rather cumbersome. Nevertheless, it is expected that these choices will provide sufficient information to elucidate the importance of the various parameters. The maximum volume load that was acceptable for PIV measurements in this facility was around 0.5–0.6%, depending on the particle material properties.

Similarly to the single-phase measurements, at least 128 image pairs were recorded at five downstream locations. This number of uncorrelated realizations was sufficient for convergence of the turbulence statistics. To enable more advanced analyses (such as conditional averaging), as many realizations as possible were collected. Owing to practical considerations (measurement time, storage space), the maximum number of realizations was 512, which corresponds to 20 Gb of raw image data for each experiment mentioned in table 4.

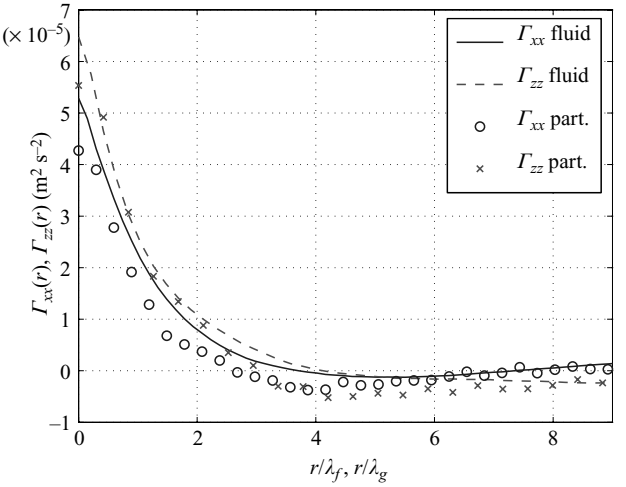

FIGURE 6. The longitudinal and transverse autocovariance functions of the fluid phase (lines) and particles (symbols) at $z/M = 56.3$. Ceramic particles with $\rho_p/\rho_f = 3.8$, $d_p = 280\,\mu\text{m}$, $\Phi_v = 0.10\%$, $\Phi_m = 0.38\%$ (Exp. 2). The separation axis has been scaled using the Taylor microscale λ obtained from the corresponding function.

3.2. *General observations*

In figure 6, an example is shown of the autocovariance function $\Gamma_{\alpha\beta}(r) \equiv \langle u'_\alpha(x)u'_\beta(x+r)\rangle$ obtained at location $z/M = 53.6$ in an experiment using ceramic particles ($d_p = 280\,\mu\text{m}$, $\rho_p = 3800\ \text{kg m}^{-3}$) with a volume load of $\Phi_v = 0.10\%$ (Exp. 2). The fluid autocovariance function was obtained from the PIV data using the row-by-row slotting approach, while the particle covariance function was obtained from the PTV data using the decomposition method (as described in § 2.4). For both cases the uncorrelated noise has been removed by replacing the value for $\Gamma(0)$ with the value obtained from extrapolation of a quadratic fit to the subsequent two data points (Benedict & Gould 1998). This method of noise removal can act as a low-pass filter if the spatial resolution is insufficient. For the single-phase case, comparison of the results after this noise removal step with earlier LDA results showed good agreement (Poelma *et al.* 2006). As this single-phase case had the most stringent resolution criteria, we assume that this noise removal did not bias our results. For the fluid phase, the noise level was usually a few percent, while for the particles this could be up to 25%. This difference can be explained by the fact that in PIV groups of tracer particles are used for velocity estimates, while in PTV a single particle is used (Poelma *et al.* 2006).

Only the separation axis in figure 6 has been made dimensionless, using the respective Taylor microscales (λ_f and λ_g for longitudinal and transverse functions, respectively) obtained from a parabolic fit. The ordinate axis has not been scaled, so that the difference in 'energy' between the particle and fluid phase can be observed directly. As can be seen in the figure, the particles have a correlation function similar to that of the fluid, albeit with a slightly lower 'energy', i.e. variance of fluctuation $\Gamma_{\alpha\alpha}^{part.}(0) = \langle u'_\alpha u'_\alpha \rangle_{part}$ which was the case for all particle types and flow conditions. This is in agreement with the fact that the Stokes numbers of the particles are finite. Based on a numerical study by Sundaram & Collins (1999*a*), we can expect a value for the particle variance that is 2–10% lower than the fluid variance for the Stokes

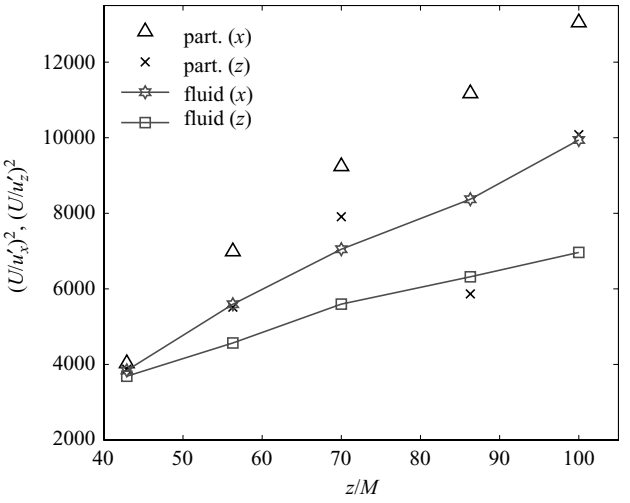

FIGURE 7. Downstream evolution of the particle-phase and fluid-phase variance for ceramic particles ($\rho_p/\rho_f = 3.8$, $d_p = 280\,\mu$m, $\Phi_v = 0.10\%$, $\Phi_m = 0.38\%$, Exp. 2).

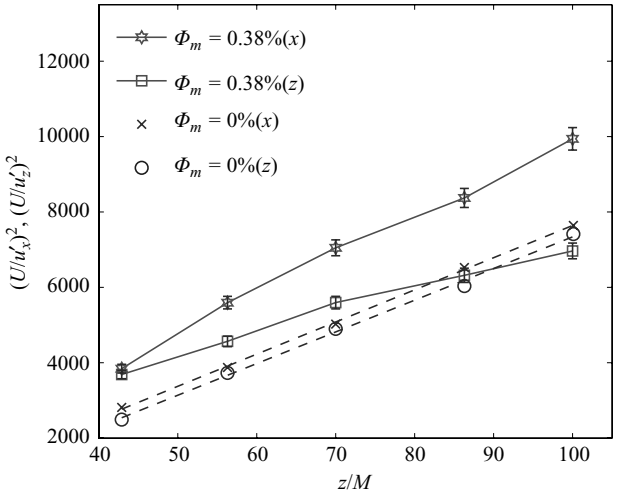

FIGURE 8. The decay of the horizontal and vertical variance of the fluid velocity fluctuations for Exp. 2 ($\rho_p/\rho_f = 3.8$, $d_p = 280\,\mu$m, $\Phi_v = 0.10\%$, $\Phi_m = 0.38\%$) and the single-phase reference case. Errorbars indicate the 95% confidence interval.

number range of the particles used. An example of the downstream evolution of the fluid and particle variances in Exp. 2 is shown in figure 7.

In figure 8, an example is given of the decay of the horizontal and vertical variance of the fluid-phase velocity fluctuations, in comparison with the single-phase reference case. The results were again obtained using ceramic particles with $d_p = 280\,\mu$m, $\rho_p/\rho_f = 3.8$ and a mass load $\Phi_m = 0.38\%$ (Exp. 2). The error bars shown represent the 95% confidence interval. The standard error of the variance is determined by the limited number of realizations of each experiment and is approximately 3%. In figure 9, the corresponding total turbulent kinetic energy (e) is shown. It was calculated by assuming that the 'out-of-plane' component, which could not measured,

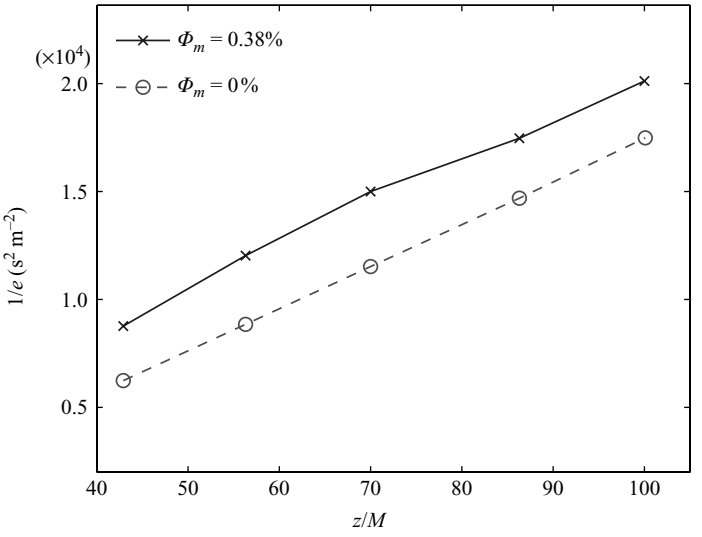

FIGURE 9. The decay of the total turbulent kinetic energy for Exp. 2 ($\rho_p/\rho_f = 3.8$, $d_p = 280\,\mu\mathrm{m}$, $\Phi_v = 0.10\%$, $\Phi_m = 0.38\%$) and the single-phase reference case.

is of the same order as the other horizontal component, i.e. $e = \frac{1}{2}(2\langle u'_x u'_x\rangle + \langle u'_z u'_z\rangle)$. Again, the single-phase results are reported as reference (dashed line).

As can be seem in figure 8, even the addition of a relatively small number of particles can have a substantial influence on the turbulence, compared to the single-phase reference case with the same centreline velocity. The two main effects are the increasing anisotropy with increasing downstream distance (z/M) and the energy at the beginning of the test section being significantly lower than the single-phase case. This type of behaviour is observed for all the particles and mass loads that were studied. The decay of the turbulent kinetic energy appears to follow a power-law decay, see e.g. the results for Exp. 2 in figure 9. Note that the reciprocal value of the energy is plotted. The slopes of the decay curves are similar for the single-phase and particle-laden case, yet the actual dissipation rate is always lower than the single-phase case for a given value of z/M.

The slower decay rate of the particle-laden cases seems in contrast to the observed lower energy at the beginning of the test section; it indicates that the initial flow conditions of the decaying turbulent flow must have changed significantly due to the addition of the particles. These are several possible explanations:

(i) *Influence of the upstream turbulence level.* Tan-atichat, Nagib & Loehrke (1982) found that increased turbulence levels of the upstream conditions could lead to different decay behaviour. Owing to the presence of particles, there can be such an increased turbulence level in the flow before the grid with respect to the single-phase flow conditions. However, Tan-atichat *et al.* (1982) found different slopes, rather than the shift in the decay that we observe in figure 9.

(ii) *Regime change in particle–fluid interaction.* In the region just behind the grid, there is significantly more turbulence than in the test section. Also, the turbulence length and time scales are smaller than during our measurements. This could lead to a different particle–fluid interaction regime (e.g. because of expected larger Stokes number). However, the scale changes are comparatively small and the Stokes numbers of the different particles vary over almost an order of magnitude. As the shift is observed for all particle types, this explanation seems unlikely.

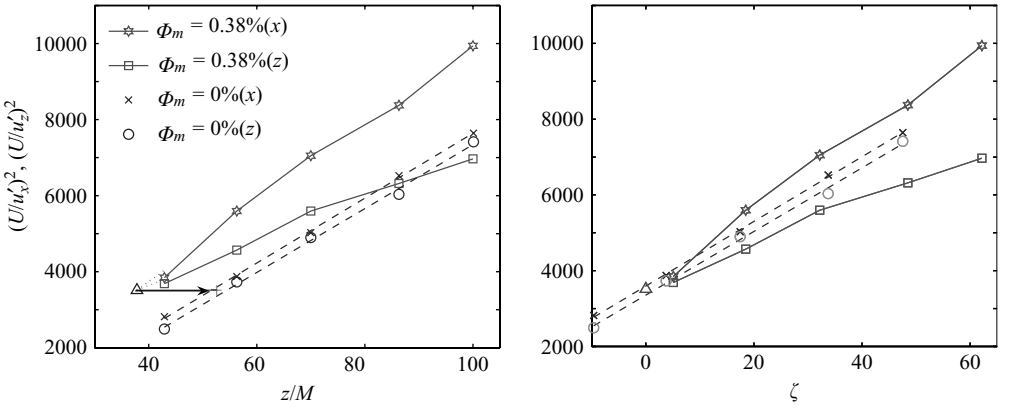

FIGURE 10. Adjustment of the virtual origin of the particle-laden case to match initial conditions. See text for details (Exp. 2, $\rho_p/\rho_f = 3.8$, $d_p = 280\,\mu$m, $\Phi_v = 0.10\%$, $\Phi_m = 0.38\%$).

(iii) *Change in the onset of decay*. Turbulence is generated at the grid by the breakdown of individual jets emerging from the grid, see for instance the well-known visualization in figure 152 of Van Dyke (1982). In single-phase flow, the traces of this breakdown process typically last up to 20 mesh spacings before the flow can be considered to be 'homogeneous, isotropic turbulence'. When particles are added, they can influence this breakdown process: an increase in the turbulence level upstream of the grid can possibly trigger a faster transition of the individual jets. This would lead to an earlier onset of the turbulent decay.

The last explanation seems the most plausible. If the decay curves are extrapolated to lower values of z/M, we can determine the so-called virtual origin–the abscissa with the horizontal axis. We find that this virtual origins shifts from $z/M = 10$ (a typical value for grid turbulence) to $z/M = -4$. Note that no correlation could be observed between the location of the new virtual origin and the suspension conditions. While the virtual origin is a theoretical concept and its physical interpretation is far from trivial, this result can suggest that the onset of turbulent decay process (e.g. the breakup and merger of individual jets emerging from the grid) starts earlier, i.e. directly at the grid.

The observed change in initial conditions complicates a straightforward comparison with the single-phase flow case and between the different particle-laden cases. To enable some sort of comparison, we propose the following adjustment method (see also figure 10):

(*a*) The data of the axial and transverse variance for the particle-laden flow are extrapolated to lower values of z/M to obtain the location at which the flow would be virtually isotropic (i.e. $\langle u'_x u'_x \rangle = \langle u'_z u'_z \rangle$, the intersection point in the graph, indicated by $\triangle$ in figure 10). This location will be referred to as the 'virtual isotropic origin' (VIO) and is denoted z^i, with turbulent kinetic energy e^i.

(*b*) In the single-phase data, the location z^{sf} where $e = e^i$ is determined. This location is indicated by $+$ in figure 10.

(*c*) The two-phase data are translated over the distance $z^{sf} - z^i$. The new dimensionless downstream distance is referred to as ζ, and for convenience the origin is set at the VIO. Note that the absolute value of ζ is only of minor importance in the following analyses, as only the decay rates will be considered.

The justification for applying this adjustment is the following: at $\zeta = 0$, the turbulent kinetic energy is identical for the particle-laden and single-phase flow. The downstream

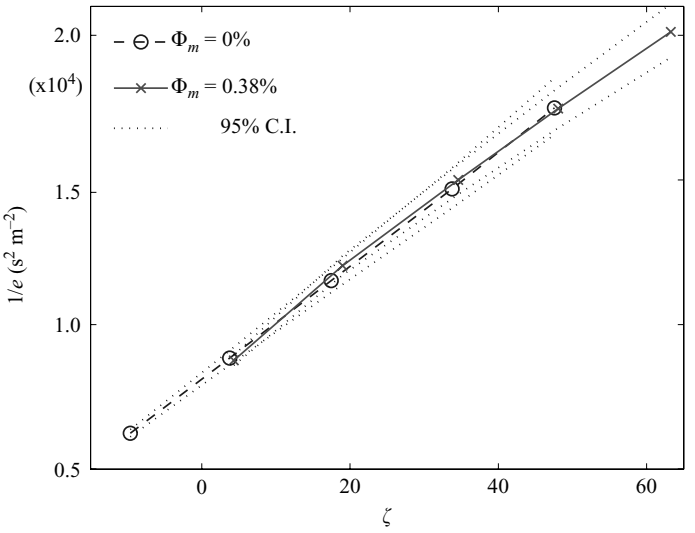

FIGURE 11. Decay of the total turbulent kinetic energy after virtual origin adjustment for the single-phase and a particle-laden case (Exp. 2, $\rho_p/\rho_f = 3.8$, $d_p = 280\,\mu$m, $\Phi_v = 0.10\%$, $\Phi_m = 0.38\%$). The 95% confidence intervals are indicated with the dotted lines.

temporal development of the flow can be studied, regardless of the absolute spatial location of the measurement locations. Obviously, the fact that the variances (and total turbulent kinetic energy) are identical at the new reference point does not mean that all the flow conditions are identical. For instance, the macroscopic length scales of the particle-laden cases are smaller by 10–20% (Poelma 2004). However, this method seems the best way to obtain direct comparisons of decay behaviour with comparable initial conditions. The need for this adjustment also highlights the fact that comparisons of particle-laden and single-phase experiments have to be done with great care. We cannot simply compare the two cases for each downstream location in an experiment and conclude that there is either attenuation or augmentation, as we need to take care that the initial conditions are identical. As we will see in the next section, we will also need to evaluate more than the turbulence level alone to fully understand the behaviour of particle-laden flows.

4. Results from the particle-laden experiments

Numerous possibilities exist to evaluate the data set obtained. In this study, the focus will be on the downstream evolution of the variance (i.e. turbulent kinetic energy) of the fluid phase. As mentioned in the previous section, all experiments showed the behaviour in figure 8: the variance of the horizontal and vertical component both show power-law decay behaviour. However, owing to a difference in decay rate, the flow becomes more and more anisotropic as it develops.

4.1. *Effect of particles on the decay rate of the turbulent kinetic energy*

If the total turbulent kinetic energy is considered using the adjustment described above, we find that the decay rate is not significantly different from the single-phase reference case, see e.g. figure 11. This was the case for all experiments with a 'subcritical' volume load (this term will be discussed in § 5.4). The confidence intervals, determined in earlier experiments (Poelma *et al.* 2006), are shown as the dotted lines.

If a linear function ($1/e = A\ z/M + B$) is fitted to the data as shown in figure 11, we find that the slope does not differ very significantly from the single-phase value (A_0): the ratio of the slopes, A/A_0, is respectively 0.94, 1.01, 1.00, 0.98 and 1.10 for Exps. 1–4 and 8.

Changes in the overall decay rate of the turbulent kinetic energy are reported in a number of publications, using either numerical simulation (Ferrante & Elghobashi 2003) or theoretical methods (Ooms & Poelma 2004). Using the same classification as introduced by Ferrante & Elghobashi (2003), all particle types can be characterized as 'ghost particles' ($St_p \equiv \tau_p/\tau_K \approx 0.1$, see table 3). For this type of particles, both Ferrante & Elghobashi (2003) and Ooms & Poelma (2004) find no change in the total decay rate, which is confirmed by our experimental data. Note that these previous studies do not take gravitational effects in account, however.

4.2. *Departure from isotropy*

Although the decay rate does not change, this does not mean that the turbulence is not affected at all. On the contrary: as could be seen in figure 8, the evolution of the individual components showed a clear trend of increasing anisotropy. Similar behaviour was observed by Geiss *et al.* (2004). A more detailed analysis of the decay of the horizontal and vertical 'energy' components† shows that the increase in horizontal decay rate is exactly half the decrease in vertical decay rate.

For instance, the data in figure 10 can be described by the linear fit:

$$\frac{U^2}{\langle u_x' u_x' \rangle} = 85\zeta + 3.6 \times 10^3 \quad \text{(horizontal)}, \tag{4.1}$$

$$\frac{U^2}{\langle u_z' u_z' \rangle} = 84\zeta + 3.4 \times 10^3 \quad \text{(vertical)}, \tag{4.2}$$

while the particle-laden case can be described by:

$$\frac{U^2}{\langle u_x' u_x' \rangle} = 100\zeta + 3.5 \times 10^3 \quad \text{(horizontal)}, \tag{4.3}$$

$$\frac{U^2}{\langle u_z' u_z' \rangle} = 60.8\zeta + 3.4 \times 10^3 \quad \text{(vertical)}. \tag{4.4}$$

This indicates that the decay of the horizontal component(s) is 18% faster than the single-phase case, while the vertical decay is 33% slower. Using the assumption of axisymmetry, we thus find that these effects largely cancel out with respect to the total decay rate. This indicates that the presence of particles merely acts as a redistribution of energy from horizontal to vertical components. The quantitative behaviour of this energy transfer is discussed in § 5.

4.3. *Change in turbulence structure*

To find out what may cause the observed anisotropy, we need to investigate how the structure of the turbulence changes as a result of the addition of the particles. This can be done by comparing integral quantities, such as the turbulent kinetic energy and integral length scale. More detailed information can be obtained by considering the turbulence power spectra and/or autocorrelation functions. First, we need to

† While turbulent kinetic energy is obviously a scalar quantity, for convenience we assume that we can split it in the individual contributions, i.e. the variances of the horizontal and vertical fluid velocity.

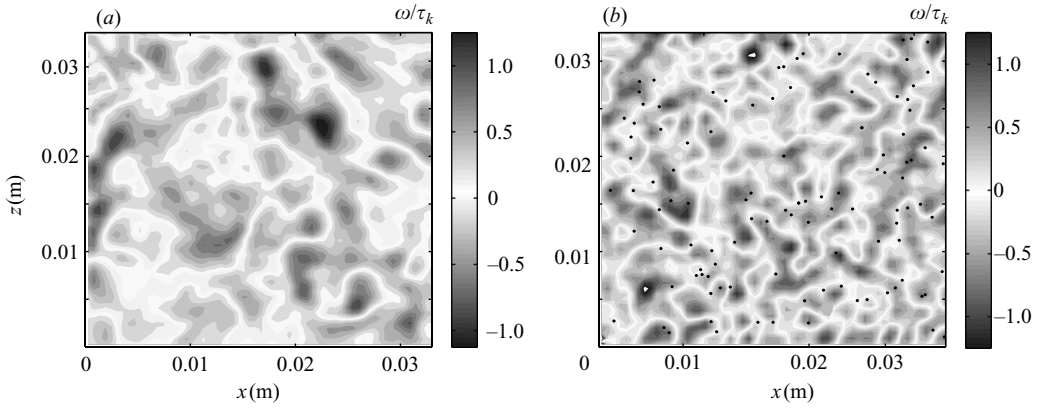

FIGURE 12. Vorticity snapshots for (*a*) the single-phase flow and (*b*) a particle-laden case ($\zeta \approx 47$). The vorticity is normalized using the local Kolmogorov time scale. Particle-laden case: Exp. 1 ($\rho_p/\rho_f = 3.8$, $d_p = 153\,\mu$m, $\Phi_v = 0.12\%$, $\Phi_m = 0.44\%$). Particle locations are indicated by the dots.

decide which cases will allow a meaningful comparison. In this study, we have chosen to compare the particle-laden case to the single-phase case for a given turbulent kinetic energy, rather than comparing the data at a fixed location. As mentioned earlier, comparing two downstream locations is far from trivial. Therefore, we will again apply the origin adjustment and compare two cases at the same value of ζ. In figure 12, we show a snapshot of the vorticity field for both the single-phase case (*a*) and a particle-laden case (*b*). The vorticity was calculated at each vector location using the circulation method (Raffel *et al.* 1998). Superimposed on this vorticity map are the particle locations, shown as the dots. The data are obtained at $z/M = 100$ for the single-phase flow and $z/M = 86.3$ for the particle-laden case (Exp. 1, $\rho_p/\rho_f = 3.8$, $d_p = 153\,\mu$m, $\Phi_v = 0.12\%$, $\Phi_m = 0.44\%$). As can be seen in figure 11, at these locations the experiments have approximately the same turbulent kinetic energy.

The vorticity field shown in figure 12 appears to have smaller length scales in the particle-laden case than in the single-phase case. When the integral length scale is calculated, we find that it decreases from 7.4 mm (single-phase) to 6.2 mm (Exp. 1), a 19% decrease. An even larger decrease can be found in the Taylor microscales: 4.3 mm (single phase) compared to 2.6 mm for the particle-laden case. While the Taylor microscales do not have a well-defined physical interpretation (though it can be stated that dissipation and transfer are in equilibrium for eddies of this size), we can postulate that the energy is present at smaller scales than the single-phase reference case. A similar reduction in length scales was found for all particle-laden experiments.

Because of the whole-field nature of the measurements, it is possible to calculate the integral length scale in both a horizontal and vertical direction. We find that the vertical length scale is always higher than the horizontal length scale, which would not be the case if the flow is isotropic. In figure 13, the ratio of the length scales calculated in the vertical and horizontal directions (Λ_z/Λ_x) is shown as a function of the anisotropy ($\langle u_z' u_z' \rangle / \langle u_x' u_x' \rangle$). This plot contains data obtained in all eight experiments, as well as the single-phase case. In some cases the effect of particles led to an increase in length scales that was so large that it was difficult to determine the integral length scale in our limited field of view. This was especially the case for

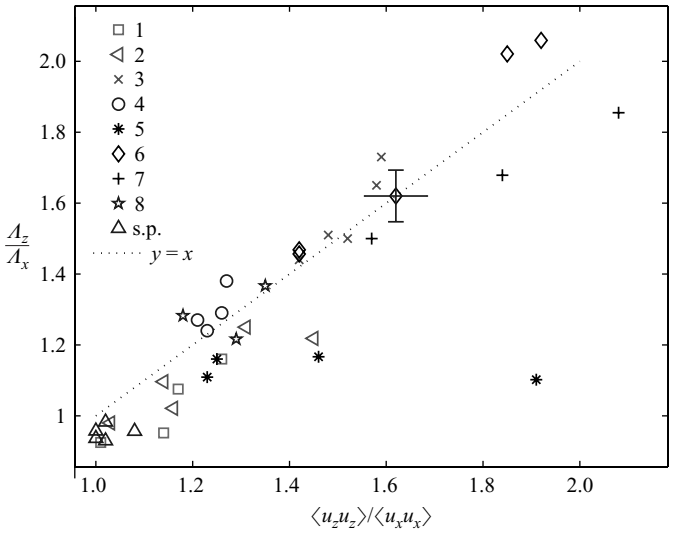

FIGURE 13. The relationship between the observed difference in horizontal and vertical integral length scales and anisotropy. The numbers refer to the experiments in table 4.

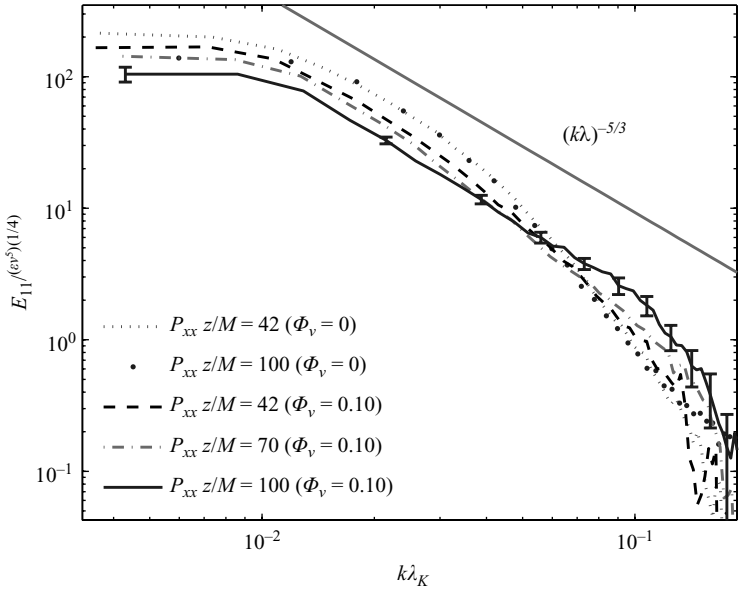

FIGURE 14. Downstream evolution of longitudinal spectrum, calculated along horizontal lines; single-phase and Exp. 2 ($\rho_p/\rho_f = 3.8$, $d_p = 280\,\mu$m, $\Phi_v = 0.10\%$, $\Phi_m = 0.38\%$).

Exp. 5, which had the highest mass load of all experiments. The reason for plotting the length scale ratio as a function of anisotropy is evident from figure 13: with an increasing anisotropy, there is also an increase in the ratio of the length scales.

Further insight into the changes of the turbulence can be given by the evolution of the turbulence power spectrum. In figure 14, the longitudinal power spectrum is shown for three downstream locations ($z/M = 42$, 70 and 100) of Exp. 2, as well as the single-phase reference case at $z/M = 42$ and $z/M = 100$. For one particle-laden

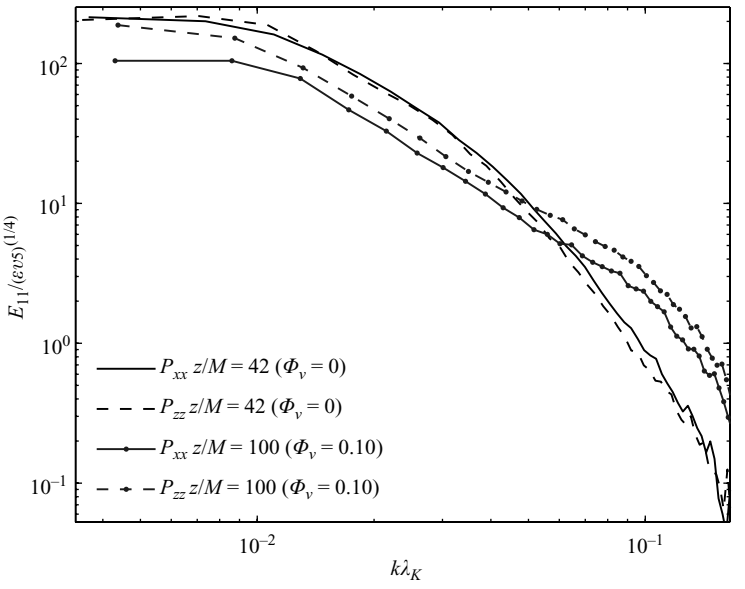

FIGURE 15. Differences between horizontal and vertical longitudinal spectra; single-phase and Exp. 2 ($\rho_p/\rho_f = 3.8$, $d_p = 280\,\mu$m, $\Phi_v = 0.10\%$, $\Phi_m = 0.38\%$).

case, the error bars are shown for a number of wavenumbers to indicate the 95% confidence interval. The data are made dimensionless using Kolmogorov scaling (Pope 2000). As can be seen in figure 14, the slope of the spectrum decreases as the flow develops: in the initial stage ($z/M = 42$), the spectrum of the particle-laden case has a shape comparable with the single-phase case. However, at the top of the test section ($z/M = 100$), the spectrum shows a region with a relatively constant slope (which is approximately $-5/3$). In contrast, the single-phase case far downstream ($z/M = 100$) closely resembles the initial spectrum for $k\lambda_k > 0.02$. The differences at large scales between the two downstream locations are due to the turbulent decay. The change in slope for the particle-laden case, which is also observed in the transverse spectrum, results in a clear 'pivoting' in the spectrum, which confirms a number of theoretical and numerical studies, as mentioned in the introduction.

The longitudinal spectra can also be calculated in the vertical direction. figure 15 shows the spectra obtained in both directions, as well as the single-phase reference case. While the general shape of the spectrum is the same for the two orientations, there is a significant difference in energy at the small wavenumbers (i.e. large scales). This is in agreement with the observed increase in anisotropy (both length scales and velocity variance).

The single-phase flow has a relatively low Reynolds number ($Re_\lambda \equiv \lambda_g u'/\nu \approx 29$), which means that there is no complete separation of large energy-containing eddies and the dissipative small eddies. Energy will not only be dissipated by the Kolmogorov eddies, but also by large-scale eddies. Therefore, the total transfer for a given wavenumber (as a result of the energy cascade plus dissipation) will be negative. This results in the observed slope that is steeper than the $-5/3$ following from Kolmogorov theory. As will be seen in the next section, there can be additional production of turbulence by the particles, which can be expected to appear at moderate wavenumber (i.e. of the order of the particle size) in the spectrum. This can explain the observed change in slope: for each wavenumber, there is now not only cascadal transfer and

dissipation, but also an extra production term due to the particles. An alternative interpretation of the change in the spectrum at large wavenumbers is an enlargement of the inertial subrange by the particles, as predicted by L'vov *et al.* (2003). This is also in agreement with the observed decrease in the Taylor microscales.

Our results for the change in spectrum mostly agree with those obtained by Yang & Shy (2005). Their experiment that is the most comparable with our work was done using particles with $St_p = 0.36$. Using these particles, they also observe a decrease at large scales and an increase at smaller scales compared to the single-phase case. However, they find a rather sudden change in the slope of the spectrum: up to the Taylor microscale, the inertial-subrange part of the single-phase and particle-laden spectra are comparable, while the slope decreases above the Taylor micro scale (indicating an increase in energy at small scales). It should be noted that their Reynolds number was significantly higher ($Re_\lambda \approx 120$ versus $Re_\lambda = 29$). The absence of a complete separation of scales in our experiment may lead to a 'merging' of the two effects. Another difference between the two studies is the different values for β, which are significantly smaller in the study by Yang & Shy (2005) compared to ours ($\beta = 0.2$ versus $\beta > 1$ for all but the neutrally buoyant particles). This means that the role of gravity is different in the two studies, making a direct comparison difficult.

4.4. *Preferential concentration effects*

The Stokes numbers of the particles used in our experiments are in the range of 0.1–0.5 (see table 3). This would make them susceptible to preferential concentration effects (Eaton & Fessler 1994). Owing to the high magnification of the measurement system, the average number of particles in the field of view is relatively low. This complicates a study of the extent of clustering. The most commonly used method is 'box counting' (Fessler, Kulick & Eaton 1994). In this method the image is subdivided in smaller regions and a histogram of the number of particles per region is determined. This histogram can then be compared to a fully random case (i.e. a Poisson distribution). In the current study, the number of particles per region is so low (100–150 particles in the field of view) that this method cannot be used. The 'dynamic range' of the number of particles in a reasonably sized box is simply too low for a meaningful interpretation.

A number of other tests was performed to see if preferential concentration effects occur. First, the distributions of particles with respect to each other was considered. Histograms of the distance to the nearest neighbouring particle were made, which did not deviate significantly from the result obtained in a completely random system. The second test consisted of conditionally sampling fluid quantities at the particle locations. Again, there seemed to be no evidence of a preferential location of particles in e.g. low-vorticity regions or regions of downward flow, as was observed by Ferrante & Elghobashi (2003). A full description of these test can be found in Poelma (2004). Because of the low number of particles, it is difficult to determine if preferential concentration effects are absent or if the particle statistics are insufficient. However, one could argue that preferential concentration effects will not be significant owing to the relatively high values of the ratio of the particle terminal velocity and the fluid fluctuations, $\beta = u_{tv}/u'$ (Yang & Shy 2005). This corresponds to a low 'residence time' of the particles in a typical vortical structure. The particles thus hardly have time to respond to e.g. vorticity fluctuations, which are strongest at Kolmogorov scales. Note that the neutrally buoyant particles have a lower value of β, yet their Stokes number is too low to exhibit preferential concentration effects.

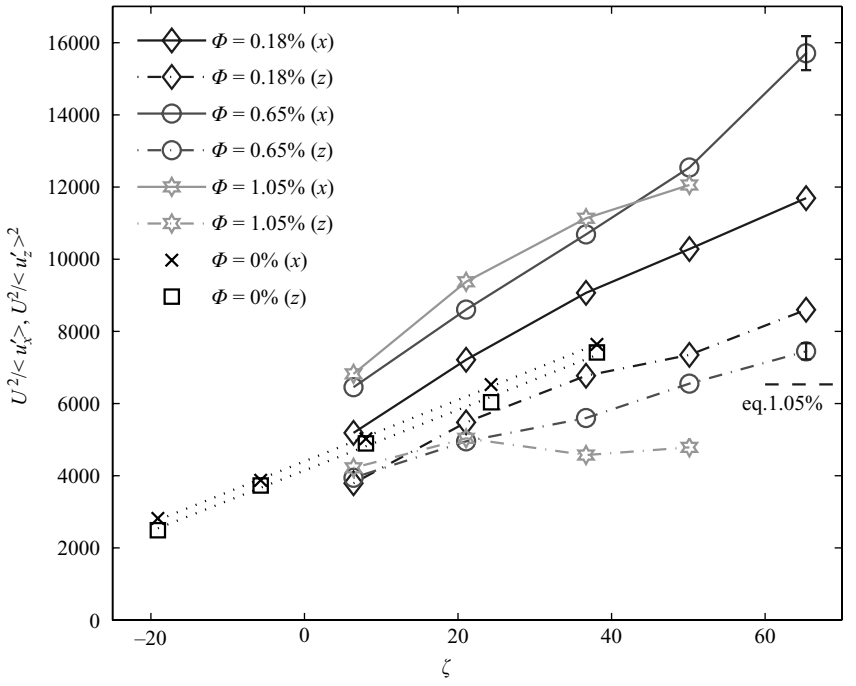

FIGURE 16. The decay of the turbulent kinetic energy for three different mass loads (Exps. 4, 3 and 6, $\rho_p/\rho_f = 2.5$, $d_p = 254\,\mu$m, $\Phi_v = 0.072\%$, 0.10% and 0.42%, $\Phi_m = 0.18\%$, 0.65% and 1.05%). The dashed line labelled 'eq.' will be discussed in a later section.

5. Discussion

As was seen in the previous section, most of the experiments followed a similar trend with an increasing anisotropy as the flow develops. To get a better understanding of this behaviour, including the influence of the suspension parameters, a number of cases will be discussed in this section. The same data will be used in a more quantitative analysis in § 5.3.

5.1. *Influence of particle load on decay behaviour*

The results from three experiments with increasing mass load of particle type P2 (Exps. 4, 3 and 6 in table 4) are shown in figure 16. Similarly, results of experiments with particle type P3 for two mass loads (Exps. 2 and 5) are shown in figure 17.

Figures 16 and 17 show that the mass load Φ_m has a strong influence on the extent of the turbulence modification by particles: as can be expected, the rate at which the flow becomes anisotropic increases with mass load. However, the mass load in itself is not sufficient for predicting modification effects. To illustrate this, two different experiments with a comparable mass load ($\Phi = 0.38\%$ and 0.44%, respectively) are shown in figure 18, for particles with the same density, but different size (153 and 280 μm, respectively). Despite the relatively small difference in mass (and volume load, since the particle density is the same) of only 15%, the number density n_p (calculated from the volume load and particle size using $n_p = 6\Phi_v/\pi d_p^3$). is more than 7 times higher owing the size difference ($n_p = 618$ versus 87cm^{-3}). Obviously, the number density in itself is also not sufficient to describe the behaviour. This is exemplified by the fact that Exps. 2 and 4 have comparable number densities (87 and 83 cm^{-3}, the lowest loads in figures 16 and 17), but show significantly different decay behaviour

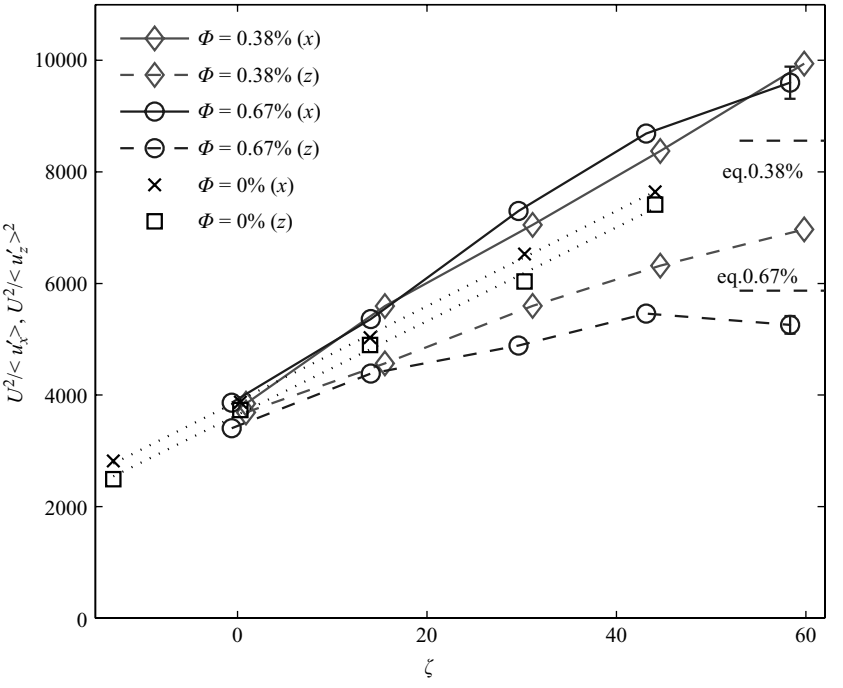

FIGURE 17. The decay of the turbulent kinetic energy for two different mass loads (Exps. 2 and 5, $\rho_p/\rho_p = 3.8$, $\Phi_v = 0.10\%$ and 0.18%, $\Phi_m = 0.38\%$ and 0.67%). The dashed line labelled 'eq.' will be discussed in a later section.

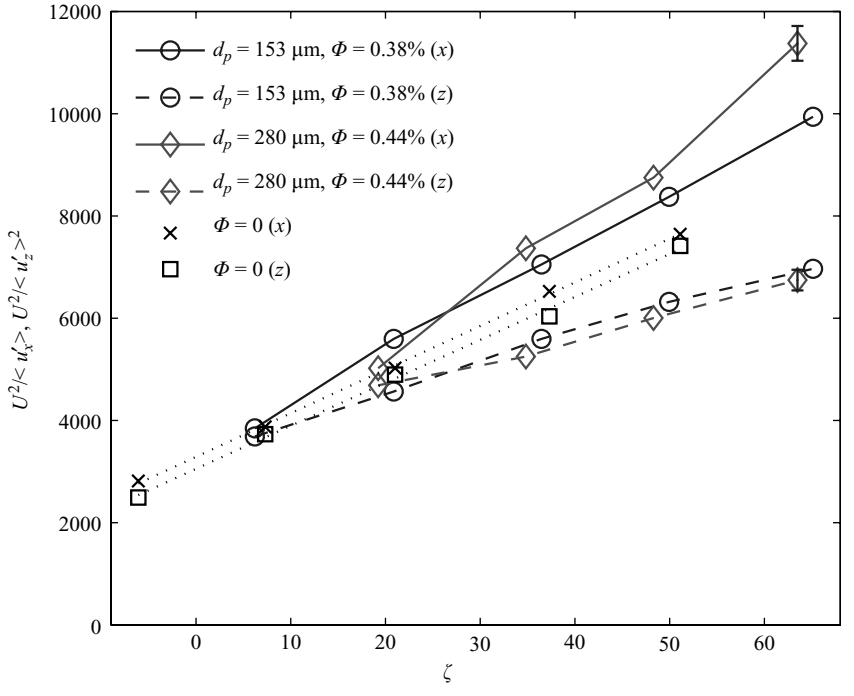

FIGURE 18. The decay of the turbulent kinetic energy for two experiments with comparable mass and volume load, but with different particle sizes (Exps. 1 and 2, $\rho_p/\rho_f = 3.8$, $d_p = 153$ and $280\,\mu$m, $\Phi_v = 0.12\%$ and 0.10%, $\Phi_m = 0.44\%$ and 0.38%.

(a 26% difference in slope for the horizontal decay). This difference in behaviour can be explained by the fact that these particle have different characteristics (i.e. density and size).

5.2. *Comparison with empirical rules*

The results described in the previous sections can be compared to the rules of thumb mentioned in the introduction and which are summarized in table 1. As can be seen in table 3, all particles are significantly smaller than the integral length scale: d_p/Λ is in the range of 0.02 (P4) to 0.08 (P1). For simplicity, the value of the single-phase result at the middle of the test section was chosen for the integral length scale, i.e. $\Lambda = 6$ mm. According to the rule of thumb suggested by Gore & Crowe (1989), particles should dampen the turbulence in these conditions. However, after the VIO adjustment we find no apparent change in energy decay, except far downstream. The latter, as will be discussed in the next section, results from the fact that far downstream the grid-generated turbulence has decayed to such a level that the particle-generated turbulence starts to dominate.

Similarly, the rules using the particle Reynolds and Stokes numbers can be evaluated. The values of Re_p, using particle size and measured terminal velocity, range from 1.3 (P0) to 30 (P1). Again, this would indicate a damping of turbulence (Elghobashi 1994), while only an increase is observed far downstream. The Stokes numbers range from 0.06 (P0) to 0.48 (P1). Also using this criterion damping, rather than enhancement, is predicted (Hetsroni 1989).

The reason for this discrepancy is the fact that the flow under consideration is significantly influenced by gravity. This is exemplified by the high ratios of settling velocities and turbulent fluctuations (i.e. β values). The rules-of-thumb must therefore consider this parameter.

5.3. *Quantitative analysis of the dissipation rate*

The effect of particles on the turbulence is here quantified by considering the change in decay behaviour, i.e. the slope of the decay curves. Intuitively, this effect can be expected to be a function of the number of particles present and their characteristics. For the former, the number density is chosen, rather than the volume or mass load. This allows a clear distinction between the amount of dispersed phase and the particle quantities. The particle number density is made dimensionless using the Kolmogorov length scale (λ_k):

$$n' \equiv \frac{6}{\pi}\frac{\Phi_v \lambda_k^3}{d_p^3}. \tag{5.1}$$

This parameter can be interpreted as the average number of particles in a dissipative eddy. The particle characteristics are usually combined to form the Stokes number. This parameter combines the particle density and size and fluid viscosity to form the 'response' time of a particle, which is made dimensionless with the Kolmogorov time scale:

$$St_p = \frac{d_p^2 \rho_p}{18 \rho_f \nu}\frac{1}{\tau_k}. \tag{5.2}$$

We postulate that the influence of the particles on the turbulence is proportional to the product of the dimensionless number density and the Stokes number, which

we will refer to as the 'Stokes load':

$$\Phi_{St} \equiv n' St_p = \frac{6}{\pi} \frac{\Phi_v \lambda_k^3}{d_p^3} \frac{d_p^2 \rho_p}{18 \rho_f \nu} \frac{1}{\tau_k} = \underbrace{\frac{\Phi_v \rho_p}{3\pi \eta d_p}}_{\text{Stokes}} \frac{\lambda_k^3}{\tau_k}. \tag{5.3}$$

In this equation, η represents the dynamic viscosity. The response time of a particle has been derived using Stokes's drag law, so the reappearance of the Stokes-like term here is not unexpected. Note that the ratio of Kolmogorov length and time scale can be expressed solely in terms of dissipation and viscosity: $\lambda_k^3/\tau_k = \nu^{7/4}\epsilon^{-1/4}$.

In order to study the influence of the particle characteristics and loads, we need to quantify the changes in the turbulence decay. The dissipation rate is not constant over the observed region as it depends on the local turbulence level. This complicates a straightforward comparison between the experiments. However, as we have observed earlier, the reciprocal of the variances shows linear behaviour. We here define the apparent dissipation rate ϵ_i' as the slope of the reciprocal values of the variance†:

$$\frac{U^2}{\langle u_i u_i \rangle} = \epsilon_i' \frac{z}{M} + C. \tag{5.4}$$

For clarity, we will omit the prime in the notation of the apparent decay rate (i.e. slope). The single-phase reference for the horizontal variance is denoted by ϵ_0. Changes in the ratio ϵ_i/ϵ_0 can now be used to quantify the change in decay behaviour, following the approach introduced by Schreck & Kleis (1993). Again, we stress the fact that the dissipation rate is a scalar quantity, but for modelling purposes we split it into three contributions. As mentioned in a previous section, the overall two-phase decay does not significantly differ from the single-phase flow, i.e. $2\epsilon_x + \epsilon_z \approx 3\epsilon_0$.

For all the experiments measurements reported in table 4, the values of ϵ_x/ϵ_0 and $n' St_p$ were calculated. If the decay followed a power law (as is the case e.g. in figure 9), a linear fit was performed using all five values of the reciprocal energy. For experiments with very high loads, the decay curve slope decreases as the flow develops (see next section). In this case, only the initial data points that showed power-law decay were used. The resulting data are shown in figure 19.

As can be seen in figure 19, there seems to be a linear relationship between the energy redistribution ϵ_x/ϵ_0 and the Stokes load:

$$\frac{\epsilon_x}{\epsilon_0} \sim 1 + n' St. \tag{5.5}$$

The proportionality constant, determined from the linear fit, is 22.7. The error bars in the horizontal direction are mainly determined by the uncertainty in the mass load (derived from the pressure drop, as described in § 2.2). The vertical error bars are dominated by the uncertainty in the variance (cf. figure 11). Also shown in figure 19 are three experiments in grid-generated turbulence by Geiss *et al.* (2004), using a constant particle size, but with increasing volume load. Using the same scaling, they collapse onto the current data set with good agreement. While the value of $n' St$ varies only over approximately an order of magnitude, it should be realized that this corresponds to a relatively wide range of experimental conditions (particle characteristics, load, air or water as continuous medium). Note that while we chose

† The 'true' dissipation rate can also be calculated from the temporal derivative of the fit of the turbulent kinetic energy: $\epsilon \equiv d\langle u_i u_i \rangle/dt = -\epsilon_i' U^3/M/(\epsilon_i' z/M + C)^2$.

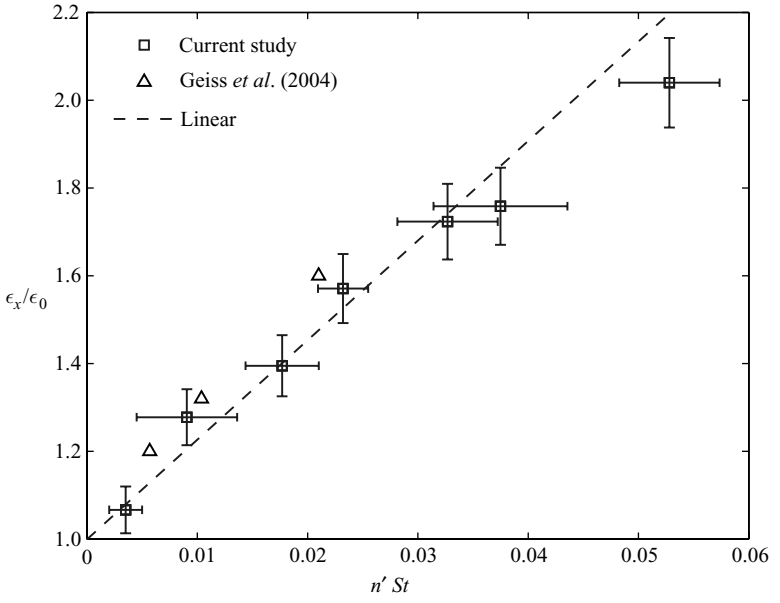

FIGURE 19. The increase in the decay rate of the horizontal variance as a function of the Stokes load $n'St_p$. The current experiments are denoted by squares, the numbers corresponds to the experiments as reported in table 4. Other data points taken from Geiss et al. (2004, △). The line indicates a linear fit through the data from the current study only.

the Kolmogorov length scale to scale the number density ($n' = n\lambda_k^3$), arguments can be given for the use of e.g. the integral length scale. Owing to the fixed ratio between integral length scales and Kolmogorov scales, either length scale will give a similar collapse on a line. However, using the Kolmogorov scale we found a slightly better agreement between our work and that of Geiss *et al.* (2004). The Reynolds number of the latter study is comparable with that of our work ($Re_M \equiv MU/\nu = 4000$ for the current experiment, 3500 and 7000 for Geiss et al.). Experiments with very different Reynolds numbers would make it possible to study the role of the choice of the length scale for the scaling.

For ϵ_z/ϵ_0, a similar linear relationship could be found (not shown). However, the proportionality constant was twice as high and negative, as expected from the fact that the total decay rate does not change. The value of the proportionality constants (approximately 23 and -40, respectively) will contain the influence of gravity. However, the current data set is not sufficient to clarify the exact formulation of this constant; more experiments with significantly different conditions (e.g. in an inclined or horizontal flow) will be needed. Alternatively, experiments similar to the work by Wells & Stock (1983) could performed that use electrically charged particles to vary the effective gravitational forces.

As the observed changes in the horizontal and vertical decay rates are not due to a true dissipation process, but rather a redistribution process, we suggest the use of the energy transfer T. We assume that this transfer is independent of the actual turbulence decay. We can then rewrite the left-hand side of equation (5.5) as

$$\frac{\epsilon_x}{\epsilon_0} = \frac{\epsilon_{2p} + T}{\epsilon_0} \approx \frac{\epsilon_0 + T}{\epsilon_0} = 1 + \frac{T}{\epsilon_0}. \tag{5.6}$$

For the energy transfer from the horizontal to vertical (i.e. gravitational) direction, we thus find

$$T \sim \epsilon_0 n' St. \tag{5.7}$$

Note that T here is the apparent energy transfer, analogous to the actual versus the apparent energy dissipation rate, as discussed in the text preceding equation (5.4).

5.4. *Turbulence generation by particles: critical versus subcritical volume loads*

For all particles heavier than water, there is a mean 'slip' velocity between the fluid and the particles. This will result in an energy input in the suspension, as potential (gravitational) energy is converted owing to the drag of the particles. Under some conditions, this can lead to an increase in turbulence. Initially, the grid-generated turbulence will be significantly higher than the turbulence generated by the particles. However, depending on the particle characteristics and load, their production can become significant. To evaluate the contribution of particle-generated turbulence, we estimate its order of magnitude. This can be done using the momentum deficit generated by each particle (Chen, Wu & Faeth 2000):

$$\Pi = n d_p^2 C_D u_{tv}^3 \tag{5.8}$$

In this equation, Π denotes the production rate of turbulent kinetic particles due to 'laminar-like turbulent wakes' of the particles (Chen *et al.* 2000; Parthasarathy & Faeth 1990). Note that in this equation, the number density per unit of mass n is used, rather than the number flux of Chen *et al.* A simplification used in equation (5.8) is the assumption that any turbulence production is proportional to the number density n. This assumes that there are no particle–particle interactions, either through collisions or particle–wake interaction. The volume loads of the current study are relatively low, so we assume that these interactions can be ignored for the purpose of the analysis in this section. The effective drag coefficient C_D can be derived from the observed terminal velocities (see table 3). This resulted in values for C_D of 21.8, 2.05, 4.24, 2.91 and 8.76 for particle types P0–P4, respectively. Note that they cannot be predicted easily *a priori* because of the unknown effects of free-stream turbulence on the drag coefficient.

In figure 20, the dissipation rate is compared to the production rate of turbulent kinetic energy by particles. The figure shows two curves for the viscous dissipation: the single-phase reference case and two particle-laden cases (Exps. 4 and 5). All three curves were derived from the experimentally determined values of the turbulent kinetic energy. For the two particle-laden experiments the production of turbulence by particles is also shown, as obtained using equation (5.8). As can be seen in this graph, there is an order of magnitude in difference in the turbulence production rates for the different experiments. For low values of z/M, the difference between dissipation and production is more than an order of magnitude. This suggests that in these early stages no effects due to particle-generated turbulence are expected. However, far downstream ($z/M = 100$) the dissipation decreases and the (constant) level of production by the particles can become significant; this is especially the case for Exp. 5. To quantify the balance between the decay of turbulence and the production of turbulence by particles (equation (5.8)), we can study their ratio:

$$\gamma = \frac{n d_p^2 C_D u_{tv}^3 \Lambda}{u'^3}. \tag{5.9}$$

In this equation, we have assumed that the dissipation scales as $\epsilon = u'^3/\Lambda$. The values for γ as a function of downstream distance z/M are shown for the same two

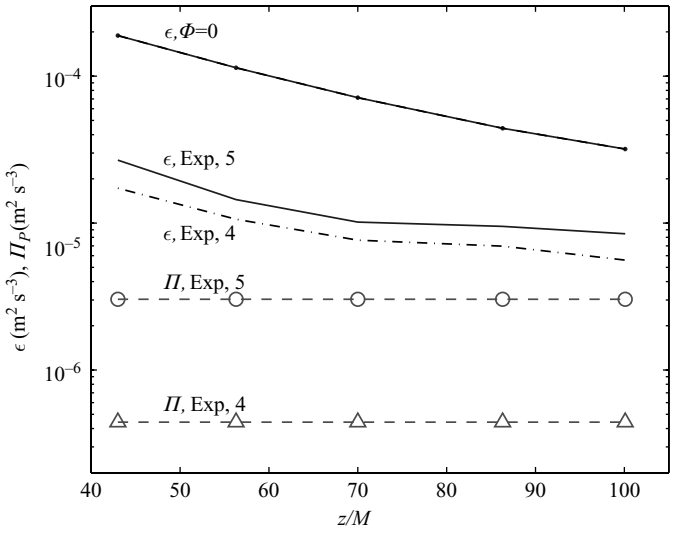

FIGURE 20. Comparison of the dissipation rate and production of turbulence by the particles. The top three curves show the dissipation of the single-phase case (ϵ, $\Phi = 0$) and two particle-laden case (ϵ, Exp. 4 and ϵ, Exp. 5). The bottom two curves represent an estimate for the production of turbulence by particles for two experiments (Π, Exps. 4,5).

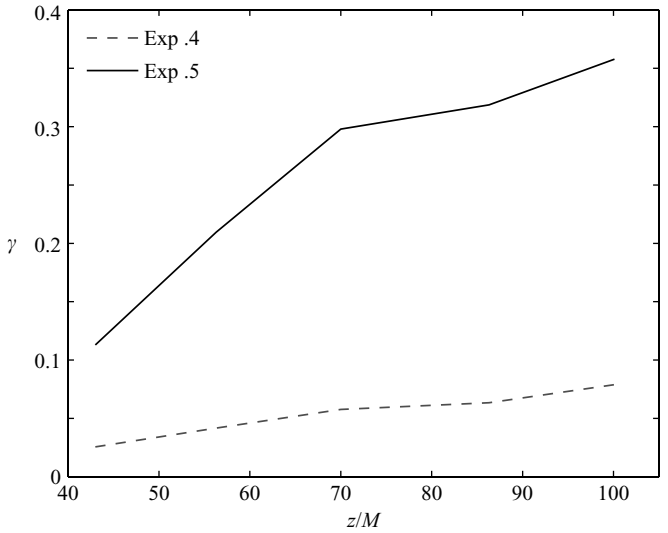

FIGURE 21. The downstream development of γ, the ratio of turbulence production by particles and the dissipation. Exp. 4: $\rho_p/\rho_f = 2.5$, $d_p = 254\,\mu\text{m}$, $\Phi_m = 0.18\%$; Exp. 5: $\rho_p/\rho_f = 3.8$, $d_p = 280\,\mu\text{m}$, $\Phi_m = 0.67\%$

experiments in figure 21. For Exp. 4, γ is well below 0.1 throughout the test section, indicating that particle-generated turbulence will not be significant. On the other hand, in Exp. 5 the value grows to 0.35–0.4 for high values of z/M. Thus turbulence production by particles can no longer be ignored in this case.

Ignoring production of turbulence at the walls, far downstream the production of turbulence by particles will be balanced by viscous dissipation, $\Pi = \epsilon$. If we again estimate the dissipation rate using u^3/Λ, we can estimate the 'equilibrium' turbulence

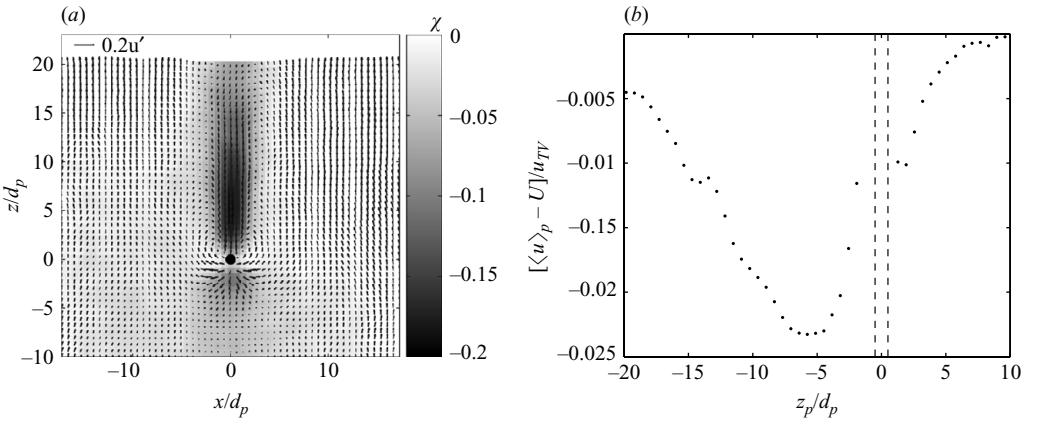

FIGURE 22. Example of a conditionally sampled fluid velocity around particle locations ($d_p = 500\,\mu$m, $\rho_p/\rho_f = 2.5$, $\Phi_v = 0.37\%$, $\Phi_m = 0.92\%$). (*a*) The two-dimensional mean velocity field, scaled with a typical fluid fluctuation, $\chi = \langle u\rangle_p/u'$. (*b*) A velocity profile at $x/d_p = 0$, scaled with the terminal velocity of the particles.

level, expressed as a typical fluid velocity fluctuation:

$$u_{eq} = (\Pi\Lambda)^{1/3}. \tag{5.10}$$

To show the meaning of this quantity, the values for some conditions are indicated in figures 16 and 17 as the short dashed line (note that it is made dimensionless using the mean velocity, i.e. U^2/u_{eq}^2). The dashed lines are labelled 'eq'. and the corresponding mass load of the experiment.

Two different cases can be distinguished: first, if the equilibrium turbulence level is very low compared to the grid-generated turbulence ($\gamma \ll 1$), the observed decay will follow a power-law decay. This behaviour is found in e.g. figure 17, for $\Phi = 0.38\%$. On the other hand, if the equilibrium level is close to the grid-generated turbulence level ($\gamma > 0.1$), the decay rate will decrease: the decay curve will asymptotically approach the equilibrium level. This behaviour can be found in e.g. figure 17 for $\Phi = 0.67\%$, especially the vertical component (circles).

This decrease in decay rate can be linked with observation in the numerical work by Ferrante & Elghobashi (2003). They calculated, with and without gravity, the influence of 'ghost' particles on a decaying turbulent flow. They found that, in the absence of gravity, the decay rate did not change compared to the single-phase flow. However, when gravity was included they found a decrease in decay rate. The former case corresponds to our results for low values of γ, where gravitational effects (i.e. production of turbulence) are overshadowed by the grid-generated turbulence, so that the decay rate is hardly affected. The latter case corresponds to higher values of γ where gravitational effects start to dominate over the decaying grid-generated turbulence, decreasing the overall decay rate.

Equation (5.8) is based on the fact that particles generate a momentum deficit in their wake, which results in additional turbulence in the fluid. For some conditions (e.g. for particles much smaller than the Kolmogorov scale), these disturbances may well be dissipated immediately. To investigate the flow around the particles, the conditionally sampled velocity around the particles has been calculated: at each detected particle location, a region in the fluid velocity result was 'cut out'. Subsequently, these were ensemble averaged. A typical result of this calculation is shown in figure 22. Part (*a*)

shows the 'two-dimensional' mean flow around a particle (500 μm glass, type P1), while Part (*b*) shows a profile at $x/d_p = 0$ of the same data set.

While figure 22 appears to show a (very large) wake region, we need to stress that this is an average over many particles in a turbulent flow: the size of the actual individual wakes is expected to be of the order of the particle size. The wake-like structure observed in the figure is the average 'footprint' of many individual wakes. This also explains why the velocities in figures 22(*a*) and 22(*b*) are relatively low (both compared to a fluid fluctuation and to the terminal velocity). However, the vertical momentum deficit contained in the large wake region is comparable to that expected in a single particle wake. It should be noted that all the measurements are taken in a single plane, while the wakes of the particles can be expected to be three-dimensional owing to the free-stream turbulence. Nevertheless, this conditional sampling exercise shows that there clearly is an effect of the particles on the fluid and that their wake disturbances are not dissipated directly.

6. Conclusions

The addition of even a moderate number of particles to grid-generated turbulence has significant effects on the development of this turbulent flow. While the overall or 'apparent' decay rate does not change significantly, there is a redistribution of energy from horizontal to vertical scales, most likely driven by the anisotropic forcing due to the slip velocity of the particles. The redistribution rate can be predicted if the non-dimensional 'Stokes load' is introduced: the product of the non-dimensional particle number density and their Stokes number. This new parameter seems a better scaling parameter than the commonly used volume or mass load, as it combines the mass load with the particle properties. Earlier experimental work reported in the literature appears to confirm the validity of the parameter, see figure 19.

The redistribution can also be observed as a change in the structure of the turbulent flow: the length scales in the horizontal and vertical direction change as the flow develops. This is accompanied by additional energy at large length scales for the vertical component. Further observations of the turbulent power spectrum confirmed the 'cross-over' effect that has been reported in a number of studies, which is due to a decrease in the observed slope compared to the single-phase flow.

While the number of particles was too low for standard clustering test ('box counting'), alternative tests indicate that the particles are randomly distributed over the flow. The explanation for this lies in the fact that the particle settling velocity is relatively high compared to a typical fluid fluctuations, so that the particles do not have time to respond to gradients.

In addition to the energy redistribution effect, the particles also generate turbulence. This is only evident when the grid-generated turbulence has decayed sufficiently. The production of turbulence by the particles can be predicted using a model based on the momentum deficit caused by the particle wakes. A study using conditional sampling showed that the particles do indeed impose such a momentum deficit on the flow and that the particle wakes are not dissipated directly. While this model seems to correctly predict the amount of turbulence that is generated, it is intriguing that this microscopic model (i.e. energy is added at the scale of a particle) appears to end up at the integral length scale in the power spectrum. An alternative explanation could be that the observed increase at low wavenumber is due to the redistribution effect, while the turbulence generated by the particles is distributed over higher wavenumbers. Further research is needed to elucidate the exact mechanisms behind this.

The results obtained in this study show that even in a seemingly simple turbulent flow (i.e. decaying homogeneous isotropic turbulence), several regimes exist: in this case initially energy redistribution and then turbulence generation by particles. This partially explains why often-used rules-of-thumb fail to predict correctly the behaviour of the flow under consideration. None of the previously available parameters takes into account all physical quantities that play a role. In particular, in the current case, the role of gravity cannot be neglected, as it is the driving force behind the observed phenomena in both regimes. To help evaluate the role of gravity, we have introduced a new parameter, γ, which represents the ratio of turbulence production of particles and the viscous dissipation of the turbulent flow. The current study has provided a number of clues that in the future should provide better ways of predicting the behaviour of particle-laden flows.

This work was supported by the Dutch Technology Foundation STW, Applied Science Division of NWO and the technology programme of the Ministry of Economic Affairs, the Netherlands (project grant DSF.4996). The authors would like to thank Professor J. C. R. Hunt for his useful comments on an earlier version of this manuscript.

REFERENCES

Aliseda, A., Cartellier, A., Hainaux, F. & Lasheras, J. C. 2002 Effect of preferential concentration on the settling velocity of heavy particles in homogeneous isotropic turbulence. *J. Fluid Mech.* **468**, 77–105.

Bagchi, P. & Balachandar, S. 2004 Response of the wake of an isolated particle to an isotropic turbulent flow. *J. Fluid Mech.* **518**, 95–123.

Batchelor, G. K. 1953 *The Theory of Homogeneous Turbulence*. Cambridge University Press.

Batchelor, G. K. & Townsend, A. A. 1948 Decay of isotropic turbulence in the initial period. *Proc. R. Soc. Lond.* **193**, 539–558.

Benedict, L. H. & Gould, R. D. 1998 Concerning time and length scale estimates made from burst-mode LDA autocorrelation measurements. *Exps. Fluids* **24**, 246–253.

Boivin, M., Simonin, O. & Squires, K. D. 1998 Direct numerical simulation of turbulence modulation by particles in isotropic turbulence. *J. Fluid Mech.* **375**, 235–263.

Boivin, M., Simonin, O. & Squires, K. D. 2000 On the prediction of gas-solid flows with two-way coupling using large eddy simulation. *Phys. Fluids* **12**, 2080–2090.

Burton, T. M. & Eaton, J. K. 2005 Fully resolved simulations of particle-turbulence interaction. *J. Fluid Mech.* **545**, 67–111.

Chen, J. H., Wu, J. S. & Faeth, G. M. 2000 Turbulence generation in a homogeneous particle-laden flow. *AIAA J.* **38**, 636–642.

Comte-Bellot, G. & Corrsin, S. 1966 The use of a contraction to improve the isotropy of grid-generated turbulence. *J. Fluid Mech.* **25**, 657–682.

Comte-Bellot, G. & Corrsin, S. 1971 Simple Eulerian time correlations of full- and narrow-band velocity signals in grid-generated isotropic turbulence. *J. Fluid Mech.* **48**, 273–337.

Deen, N. G., Hjertager, B. H. & Solberg, T. 2000 Comparison of PIV and LDA measurement methods applied to the gas-liquid flow in a bubble column. *Proc. 10th Intl Symp. on Appl. of Laser Techniques to Fluid Mech., Lisbon, Portugal.* p. 38.5.

Eaton, J. K. & Fessler, J. R. 1994 Preferential concentration of particles by turbulence. *Intl J. Multiphase Flow* **20**, 169–209.

Elghobashi, S. 1994 On predicting particle-laden turbulent flows. *Appl. Sci. Res.* **52**, 309–329.

Elghobashi, S. & Truesdell, G. C. 1993 On the two-way interaction between homogeneous turbulence and dispersed solid particles. I: Turbulence modification. *Phys. Fluids* **5**, 1790–1801.

Ferrante, A. & Elghobashi, S. 2003 On the physical mechanisms of two-way coupling in particle-laden isotropic turbulence. *Phys. Fluids* **15**, 315–329.

Fessler, J. R., Kulick, J. D. & Eaton, J. K. 1994 Preferential concentration of heavy particles in a turbulent channel flow. *Phys. Fluids* **6**, 3742–3749.

Geiss, S., Dreizler, A., Stojanovic, Z., Chrigui, M., Sadiki, A. & Janicka, J. 2004 Investigation of turbulence modification in a non-reactive two-phase flow. *Exps. Fluids* **36**, 354–354.

Gore, R. A. & Crowe, C. T. 1989 Effect of particle size on modulating turbulent intensity. *Intl J. Multiphase Flow* **15**, 279–285.

Hetsroni, G. 1989 Particle-turbulence interaction. *Intl J. Multiphase Flow* **15**, 735–746.

Hussainov, M., Karthushinsky, A., Rudi, Ü., Shcheglov, I., Kohnen, G. & Sommerfeld, M. 2000 Experimental investigation of turbulence modulation by solid particles in a grid-generated vertical flow. *Intl J. Heat Fluid Flow* **21**, 365–373.

Kiger, K. T. & Pan, C. 2000 PIV technique for the simultaneous measurement of dilute two-phase flows. *Trans. ASME: J. Fluids Engng* **122**, 811–818.

Kiger, K. T. & Pan, C. 2002 Suspension and turbulence modification effects of solid particulates on a horizontal turbulent channel flow. *J. Turbulence* **3**, no. 019.

Kussin, J. & Sommerfeld, M. 2002 Experimental studies on particle behaviour and turbulence modification in horizontal channel flow with different wall roughness. *Exps. Fluids* **33**, 143–159.

Landau, L. D. & Lifshitz, E. M. 1987 *Fluid Mechanics*. Pergamon.

Lee, K., Faeth, G. M. & Chen, J.-H. 2003 Properties of particle-generated turbulence in the final-decay period. *AIAA J.* **41**, 1332–1340.

Lindken, R. & Merzkirch, W. 2002 A novel PIV technique for measurements in multiphase flows and its application to two-phase flows. *Exps. Fluids* **33**, 814–825.

L'vov, V. S., Ooms, G. & Pomyalov, A. 2003 Effect of particle inertia on the turbulence in a suspension. *Phys. Rev.* E **67**, 046314.

Maxey, M. R. & Riley, J. J. 1983 Equation of motion for a small rigid sphere in nonuniform flow. *Phys. Fluids* **26**, 883.

Ooms, G. & Poelma, C. 2004 Comparison between theoretical predictions and DNS-results for a decaying turbulent suspension. *Phys. Rev.* E **69**, 056311.

Ooms, G. & Poesio, P. 2005 Effect of particle inertia and gravity on the turbulence in a suspension. *Phys. Fluids* **17**, 1–12.

Parthasarathy, R. N. & Faeth, G. M. 1990 Turbulence modulation in homogeneous dilute particle-laden flow. *J. Fluid Mech.* **220**, 485–514.

Poelma, C. 2004 Experiments in particle-laden turbulence. PhD thesis, Delft University of Technology.

Poelma, C. & Ooms, G. 2006 Particle-turbulence interaction in a homogeneous, isotropic turbulent suspension. *Appl. Mech. Rev.* **59**, 78–90.

Poelma, C., Westerweel, J. & Ooms, G. 2006 Turbulence statistics from optical whole-field measurements in particle-laden turbulence. *Exps. Fluids* **40**, 347–363.

Pope, S. 2000 *Turbulent Flows*. Prentice-Hall.

Raffel, W., Willert, C. & Kompenhans, J. 1998 *Particle Image Velocimetry: A Practical Guide*. Springer.

Schreck, S. & Kleis, S. J. 1993 Modification of grid-generated turbulence by solid particles. *J. Fluid Mech.* **249**, 665–688.

Sirivat, A. & Warhaft, Z. 1983 The effect of a passive cross-stream temperature gradient on the evolution of temperature variance and heat flux in grid turbulence. *J. Fluid Mech.* **128**, 323–346.

Sommerfeld, M., Tsuji, T. & Crowe, C. T. 1997 *Multiphase Flows with Droplets and Particles*. CRC Press.

Squires, K. D. & Eaton, J. K. 1990 Particle response and turbulence modification in isotropic turbulence. *Phys. Fluids* **2**, 1191–1203.

Sundaram, S. & Collins, L. 1999*a* Collision statistics in an isotropic particle-laden turbulent suspension. Part 1. Direct numerical simulations. *J. Fluid Mech.* **335**, 75–109.

Sundaram, S. & Collins, L. 1999*b* A numerical study of the modulation of isotropic turbulence by suspended particles. *J. Fluid Mech.* **379**, 105–143.

Tan-atichat, J., Nagib, H. M. & Loehrke, R. I. 1982 Interaction of free-stream turbulence with screens and grids. *J. Fluid Mech.* **114**, 501–528.

Ten Cate, A., Derksen, J. J., Portela, L. M., Kramer, H. J. M. & Van den Akker, H. E. A. 2004 Fully resolved simulations of colliding monodisperse spheres in forces isotropic turbulence. *J. Fluid Mech.* **519**, 233–271.

Tsuji, Y. & Morikawa, Y. 1982 LDV measurements of an air-solid two-phase flow in a horizontal pipe. *J. Fluid Mech.* **120**, 385–409.

Tummers, M. J. & Passchier, D. M. 2001 Spectral analysis of biased LDA data. *Meas. Sci. Tech.* **12**, 1641–1650.

Van Atta, C. W. & Chen, W. Y. 1968 Correlation measurements in grid turbulence using digital harmonic analysis. *J. Fluid Mech.* **34**, 497–515.

Van Dyke, M. 1982 *An Album of Fluid Motion*. Stanford, USA: Parabolic Press.

Wells, M. R. & Stock, D. E. 1983 The effect of crossing trajectories on the dispersion of particles in a turbulent flow. *J. Fluid Mech.* **136**, 31–62.

Westerweel, J. 1993 Digital particle image velocimetry. PhD thesis, Delft University of Technology.

Willert, C. E. 1997 Stereoscopic digital particle image velocimetry for application in wind tunnel flows. *Meas. Sci. Tech.* **8**, 1465–1479.

Willert, C. E. & Gharib, M. 1991 Digital particle image velocimetry. *Exps. Fluids* **10**, 181–193.

Yang, T. S. & Shy, S. S. 2005 The settling velocity of heavy particles in an aqueous near-isotropic turbulence. *J. Fluid Mech.* **526**, 171–216.

Yarin, L. P. & Hetsroni, G. 1994 Turbulence intensity in dilute two-phase flow-3; the particles-turbulence interaction in dilute two-phase flow. *Intl J. Multiphase Flow* **20**, 27–44.

Yuan, Z. & Michaelides, E. E. 1992 Turbulence modulation in particulate flows - a theoretical approach. *Intl J. Multiphase Flow* **18**, 779–785.